YALE PEABODY MUSEUM

JOURNAL OF MARINE RESEARCH

The *Journal of Marine Research,* one of the oldest journals in American marine science, published important peer-reviewed original research on a broad array of topics in physical, biological, and chemical oceanography vital to the academic oceanographic community in the long and rich tradition of the Sears Foundation for Marine Research at Yale University.

An archive of all issues from 1937 to 2021 (Volume 1–79) are available through EliScholar, a digital platform for scholarly publishing provided by Yale University Library at https://elischolar.library.yale.edu/.

Requests for permission to clear rights for use of this content should be directed to the authors, their estates, or other representatives. The *Journal of Marine Research* has no contact information beyond the affiliations listed in the published articles. We ask that you provide attribution to the *Journal of Marine Research.*

Yale University provides access to these materials for educational and research purposes only. Copyright or other proprietary rights to content contained in this document may be held by individuals or entities other than, or in addition to, Yale University. You are solely responsible for determining the ownership of the copyright, and for obtaining permission for your intended use. Yale University makes no warranty that your distribution, reproduction, or other use of these materials will not infringe the rights of third parties.

Internal tides on the East China Sea Continental Slope

by Ren-Chieh Lien[1,2,3], Thomas B. Sanford[1,3], Sen Jan[4],
Ming-Huei Chang[5] and Barry B. Ma[1]

ABSTRACT

Strong semidiurnal internal tides are observed on the continental slope of the East China Sea (ECS) using an array of subsurface moorings and EM-APEX floats. A Princeton Ocean Model (POM) is used to simulate the effects of stratification profiles on the generation and propagation of M_2 internal tides; model simulations are compared with observations. On the ECS continental slope northeast of Taiwan, the semidiurnal barotropic tidal current flows nearly perpendicular to the shelf break and continental slope, favoring the generation of internal tides. Both the critical slope analysis and numerical model results suggest multiple generation sites on the continental slope, shelf break and around North Mien-Hua Canyon. Unique high-wavenumber semidiurnal internal tides with a dominant vertical scale of ∼100 m are found on the continental slope. The high-wavenumber semidiurnal internal tides appear in a form of spatially coherent shear layers across the ECS slope. They propagate vertically both upward and downward. Patches of strong energy and shear at a typical vertical scale of $O(50\text{ m})$ are present at the intersections of the upward and downward propagating high-wavenumber internal tides. The strong shear of high-wavenumber semidiurnal tides could play an important role in triggering shear instability on the ECS slope. The semidiurnal internal tidal energy flux, primarily in low wavenumbers, on the ECS slope, exhibits strong temporal and spatial variations. The observed depth integrated energy flux is 3.0–10.7 kW m^{-1}, mostly seaward from the continental shelf/slope. The POM model predicts similar seaward energy fluxes at a slightly weaker magnitude, 1.0–7.2 kW m^{-1}. The difference may be due to the absence of mesoscale processes in the model, e.g., the Kuroshio Current and eddies, the assumed horizontally uniform stratification profiles, insufficient model resolution for the abrupt canyon bathymetry, and the lack of the other major semidiurnal tidal constituent, S_2, in the model. On the ECS slope, the total energy in the internal wave continuum, between 0.3 cph (beyond semidiurnal tidal harmonics) and the buoyancy frequency, is 6-13 times that of the Garrett–Munk model, presumably as a result of the energy cascade from strong inertial waves and internal tides in the region.

1. Applied Physics Laboratory, University of Washington, Seattle, WA, USA.
2. Corresponding author *e-mail: lien@apl.washington.edu*
3. School of Oceanography, College of the Environment, University of Washington, Seattle, WA, USA.
4. Institute of Oceanography, National Taiwan University, Taipei, Taiwan.
5. National Taiwan Ocean University, Keelung, Taiwan.

1. Introduction

Internal tides are generated as barotropic tides flow over abrupt topography, such as submarine ridges, shelf breaks or canyon rims. Therefore, part of the barotropic tidal energy is converted to internal tides. The vertical shear associated with internal tides may trigger interior turbulence mixing via shear instability. Internal tides propagate horizontally and vertically, and at critical bottom slopes they may be amplified and dissipated (Eriksen, 1982). The most recent internal tide experiment at Hawaii (HOME, Lee et al., 2006) concluded that most of the energy propagates away from the generation site and a small portion dissipates locally (Klymak et al., 2006). Jan et al. (2009) performed a numerical study of internal tides in Luzon Strait and concluded nearly 50% (10 GW) of internal tidal energy is dissipated locally due to the unique double submarine ridges. Understanding internal tide generation and propagation near the continental shelf and slope is particularly important to studies of mixing and water mass exchange between continental shelves/slopes and the open ocean.

In a discussion of the generation of internal tides over ridges and continental shelf breaks, Garrett and Kunze (2007) suggested that low-mode internal tides might be generated at a ridge if its height is comparable to the nodal points of low-mode internal tides. On a continental shelf break, a superposition of baroclinic modes will be generated, forming the internal tidal beam. Low-mode internal tides propagate faster than high-mode internal tides. High-mode internal tides are either advected by the background current because of their slow propagation speed, or are dissipated locally due to their high vertical shear. Enhanced shear instability and turbulence mixing have been observed in internal tidal beams (Lueck and Mudge, 1997; Lien and Gregg, 2001).

Internal waves observed in the open ocean often agree with the internal wave model spectrum constructed by Garrett and Munk (1972; 1975), and later modified by Cairns and Williams (1976), and hereafter referred to as GM. A disparity is expected near the generation sites of internal waves. Hotchkiss and Wunsch (1982) reported that the internal wave spectral level in the Hudson Canyon, near generation sites of internal waves, exceeds that of the GM spectrum.

Most internal wave energy is derived either from inertial waves or internal tides. Through wave–wave interactions, energy from internal tides and inertial waves cascades into the internal wave continuum, and eventually dissipates into turbulence. Because of strong internal tides and inertial waves generated by monsoon and tropical cyclones on the ECS continental slope, we anticipate internal wave energy to be higher than the GM level.

Here, we present observations from the ECS continental slope near a submarine canyon northeast of Taiwan. The experiment, platforms, instruments and measurements are described in Section 2. Results of the spectral analysis and consistency relation tests for linear internal waves are presented in Section 3. Internal tide generation sites and ray tracing are discussed in Section 4. The vertical and horizontal propagation of internal tides are presented in Section 5. In Section 6, we compute internal tidal energy fluxes from EM-APEX float and mooring observations. Results of a numerical model study of internal tides on the ECS are presented in Section 7, which is followed by a summary in Section 8.

2. Experiment and Measurements

a. Experiment

Six subsurface moorings were deployed northeast of Taiwan to study intrusions of the Kuroshio Current and internal tides (Fig. 1). Each mooring was equipped with one upward-looking Teledyne RDI 75-kHz Long Ranger ADCP, measuring vertical profiles of velocity, and nine SBE37 CTDs, measuring temperature, salinity and pressure (Fig. 1d). Mooring positions, water depths, sensor depths and measurement periods are summarized in Table 1. The Long Ranger pings every 10 s with a vertical bin size of 8 m. Because of the side lobe reflection at the sea surface, velocity measurements within 50 m from the sea surface are contaminated. Valid velocity measurements were taken typically between ∼500 m and 50 m depth. CTDs take measurements every 10 s. All CTD sensors have pumps to minimize salinity spiking.

One mooring was located on the I-Lan ridge, on the path of the Kuroshio, one mooring in the middle of the continental slope between Mien-Hua and North Mien-Hua (NMH) canyons, and the other four moorings on the two sides of the western branch of NMH Canyon (Figs. 1 and 2). Moorings were deployed on Aug. 3–5, 2009, before Typhoon Morakat passed south of I-Lan Ridge on Aug. 6, and recovered on Sept. 13–15, 2009. The total period of mooring measurements was about 40 days, covering ∼2.9 fortnightly tidal cycles (Fig. 3a).

Six EM-APEX floats (Sanford et al., 2005) were deployed in the vicinity of NMH Canyon (Fig. 1c and Fig. 2) between Aug. 26 and Sept. 4, 2009. Floats profiled vertically between the sea surface and the sea floor taking measurements of temperature, salinity, pressure and horizontal velocity. When floats surfaced, they transmitted data via Iridium satellite. The floats' vertical descent and ascent speeds were 0.1–0.2 m s^{-1}. The mean vertical resolution of velocity and CTD measurements is ∼4 m. All floats drifted predominantly southward at a speed of ∼0.5 m s^{-1} (Fig. 1), presumably advected by the Kuroshio Countercurrent (Gawarkiewicz et al., 2011). As floats drifted beyond the experiment area, they were recovered and redeployed near the NMH Canyon again. Five of six floats were recovered and redeployed three times, i.e., three missions, and the sixth float had only one mission, for a total of 16 missions. A total of 395 vertical profiles of EM-APEX float measurements were obtained over the two-week period.

b. Measurements

Barotropic tides on the ECS continental slope are predicted using the Oregon State University (OSU) TOPEX/Poseidon global tidal model (TPXO) (Egbert and Erofeeva, 2002) with two major semidiurnal constituents, M_2 and S_2, and two major diurnal constituents, K_1 and O_1. Apparent fortnightly cycles of semidiurnal and diurnal tides are present on the ECS slope, with maximum surface elevation amplitudes of 0.6 m for semidiurnal tides and 0.4 m for diurnal tides (Fig. 3a and 3b). The barotropic semidiurnal tide peak amplitudes were on Aug. 8, Aug. 22 and Sept. 5; the barotropic diurnal tide peaks were on Aug. 3,
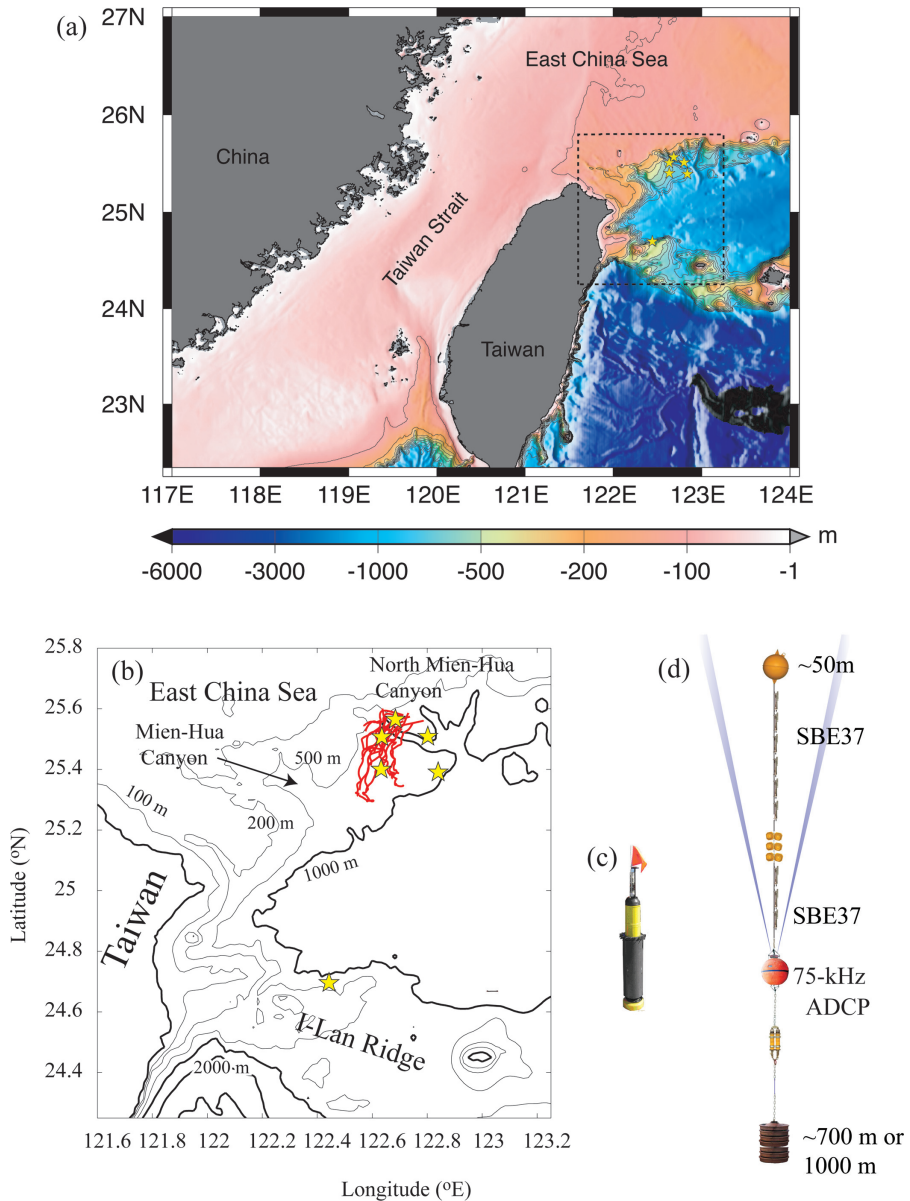
Figure 1. (a) Bathymetry chart surrounding Taiwan, (b) bathymetry detail from within the dashed rectangle in (a). The 500 m resolution bathymetric data were provided by the Ocean Data Bank of Taiwan's National Science Council. Thick black curves are isobaths with 1,000 m interval. Thin black curves are isobaths of 100, 200 and 500 m. Yellow stars represent mooring positions. Red curves represent trajectories of EM-APEX floats. (c) Photo of EM-APEX float. (d) Mooring configuration.

Table 1. Mooring measurement periods, positions, water depths and sensor depths.

| Mooring Period (2009)	Lat/Lon	Water Depth (m)/ Upward-Looking ADCP Transducer Depth (m)	CTD Sensors Depth (m)
QP1 08/03–09/12	24° 41.820′N 122° 26.568′E	685/514	55, 75, 104, 143, 191, 245, 315, 391, 481
QP2 08/04–09/13	25° 24.078′N 122° 37.938′E	678/508	28, 48, 78, 118, 167, 228, 296, 376, 466
QP3 08/04–09/13	25° 23.496′N 122° 50.394′E	906/516	42, 62, 92, 131, 180, 240, 309, 387, 477
QP4 08/05–09/13	25° 30.570′N 122° 48.138′E	903/513	38, 59, 88, 127, 176, 235, 305, 384, 474
QP5 08/05–09/13	25° 33.960′N 122° 41.064′E	678/508	28, 49, 79, 119, 169, 229, 297, 377, 467
QP6 08/05–09/14	25° 30.474′N 122° 38.088′E	678/509	35, 55, 86, 126, 176, 235, 305, 385, 475
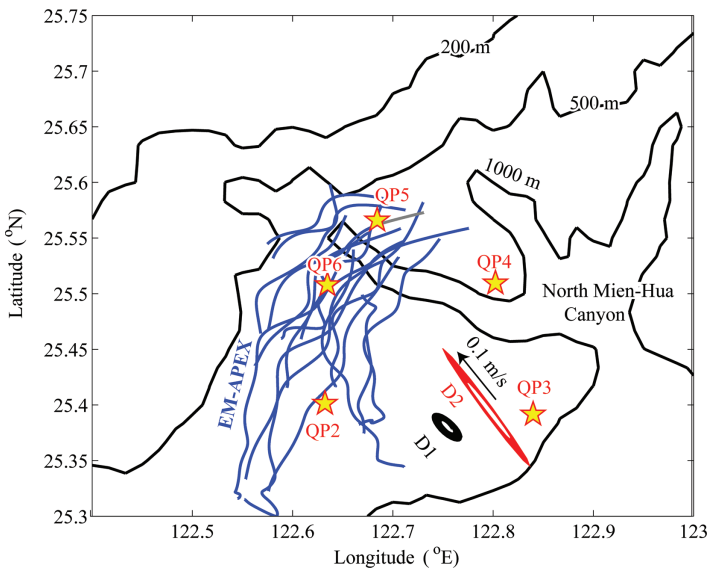
Figure 2. Close-up bathymetry chart and observational experiment on the East China Sea continental slope. Black contours show isobaths of 200 m, 500 m and 1,000 m. Yellow stars represent moorings QP2, QP3, QP4, QP5 and QP6. Blue curves show trajectories of EM-APEX floats. Diurnal (D1) and semidiurnal (D2) barotropic tidal current ellipses computed from OSU TOPEX/Poseidon Global Inverse Solution (TPXO) are shown as black and red ellipses with the velocity scale 0.1 m s^{-1} labeled.
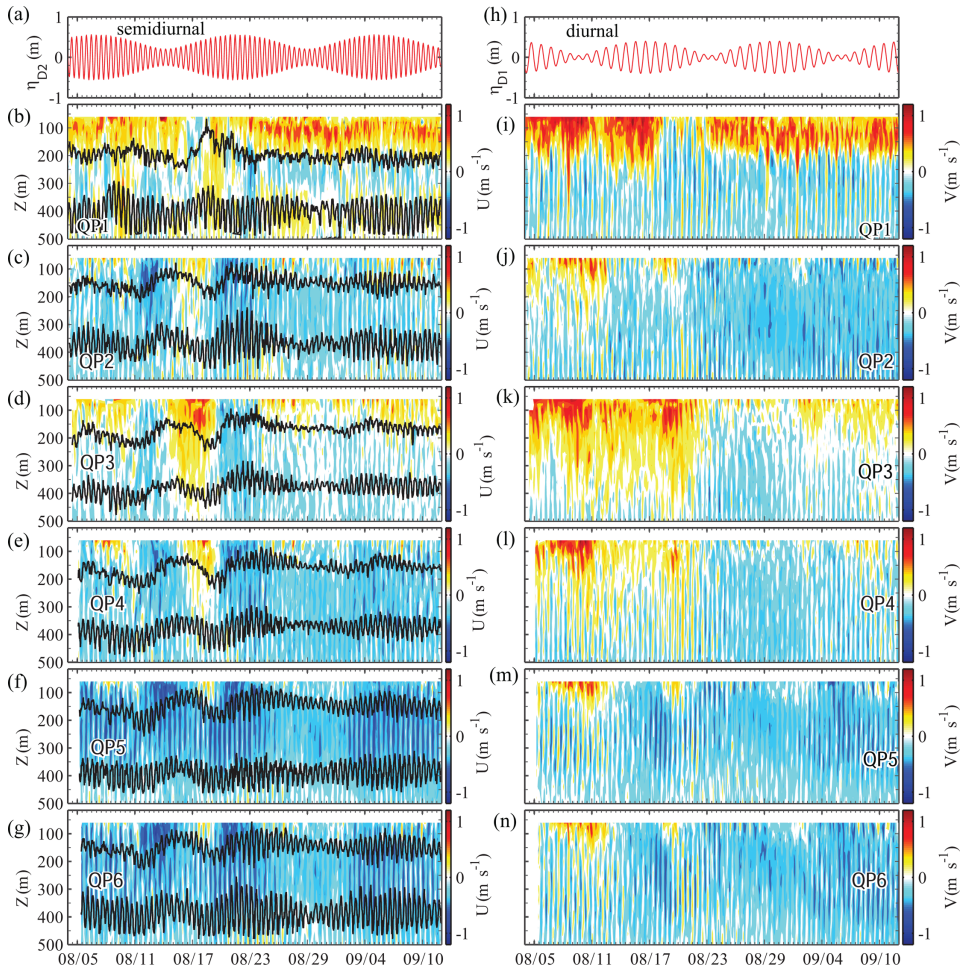
Figure 3. (a) and (h) Time series of semidiurnal (D2) and diurnal (D1) sea level variations on the East China Sea continental slope computed using OSU TOPEX/Poseidon Global Inverse Solution (TPXO) with two major diurnal and two major semidiurnal constituents. (b)–(g) and (i)–(n) Contour plots of zonal and meridional velocity observations on moorings QP1–6. Black curves in (b)–(g) represent isopycnals at the equilibrium depths of 200 m and 400 m.

17 and 31. The major axis of the semidiurnal barotropic tidal current ellipse was $\sim320°$T (true degrees); the diurnal barotropic tidal current ellipse is $\sim310°$T. They were nearly perpendicular to isobaths (Fig. 2), suggesting potential interaction with topography. The semidiurnal barotropic tidal current amplitude was 0.05–0.12 m s^{-1} during the observation period. The diurnal barotropic tidal current was less than 0.03 m s^{-1}.

Temporal and depth variations of horizontal velocity and vertical displacements of potential density $\sigma_\theta = 25.4$ and 26.4 kg m^{-3} show signatures of the Kuroshio, 4-5-day

low-frequency fluctuations, and internal tides (Fig. 3). Mooring QP1 was located on the main path of the Kuroshio. A strong northeastward current, >1 m s^{-1}, a signature of the Kuroshio, was present in the upper 200 m, except between Aug. 18 and 23. A slightly weaker northeastward current was also observed in the upper 200 m at moorings QP3 and QP4, which were located on the edge of the Kuroshio path. Between Aug. 7 and 12, a north-ward current was observed at QP2, QP5 and QP6, due to the Kuroshio intrusion induced by Typhoon Morakat (Gawarkiewicz et al., 2011).

Horizontal velocity and isopycnal displacement observations show 4-5-day low-frequency fluctuations at moorings QP2—6 before Aug. 23. An eastward current was accompanied by depressed isopycnals, and a westward current was accompanied by elevated isopycnals. These 4-5-day fluctuations could be a signature of topographic Rossby waves generated as the Kuroshio interacts with the continental slope. Kuroshio intrusions may be reinforced by such topographic Rossby waves (Qui and Imasato, 1990).

Isopycnal displacements and horizontal velocities show semidiurnal tidal variations, stronger at moorings QP1, QP2 and QP6, and weaker at QP3, QP4 and QP5, presum-ably because they are farther away from the generation sites of semidiurnal internal tides. The maximum isopycnal amplitude, ~100 m, occurred around Aug. 22, corresponding to the peak of the semidiurnal barotropic tidal forcing.

3. Spectral analysis and energy distribution

Frequency spectra of zonal and meridional velocities, clockwise (CW) and counterclock-wise (CCW) velocities are computed and compared with the GM spectral model (Appendix A) (Garrett and Munk, 1972, 1975; Cairns and Williams, 1976). The GM internal wave spec-trum represents an average equilibrium internal wave state in the ocean. Observed velocity spectra $\Phi(\omega)$ are computed at 8 m vertical bins between 50 and 500 m depth. They are WKB normalized, $\Phi(\omega)N_0/N(z)$ by the local buoyancy frequency $N(z)$ at each depth, where N_0 is the reference buoyancy, chosen to be 3 cph as used in GM. WKB normalized spectra at all depths are averaged to yield a mean WKB normalized spectrum at each mooring site (Fig. 4).

Narrow spectral peaks are found at semidiurnal (D2) frequency. Broader spectral peaks are found centering between diurnal (D1) frequency, 0.042 cph and 0.039 cph for K_1 and O_1 constituents, respectively, and inertial (f) frequency 0.036 cph. D1 and inertial frequencies are nearly inseparable at this latitude. Semidiurnal spectral peaks are at least three times larger than peaks between D1 and f. Spectral peaks at higher tidal harmonics also exist, suggesting nonlinear internal tides. van Haren et al. (2002) reported similar spectral peaks at higher tidal harmonics on the continental slope of the Bay of Biscay, and showed a spectral slope close to –1 between f and higher tidal harmonics followed by a steep spectral slope at higher frequencies. We also find a slower than –2 spectral slope between f and higher tidal harmonics.

At frequencies beyond tidal frequencies and higher harmonics, i.e., within the internal wave continuum, spectra exhibit a –2 slope, identical to the GM. However, spectral levels of
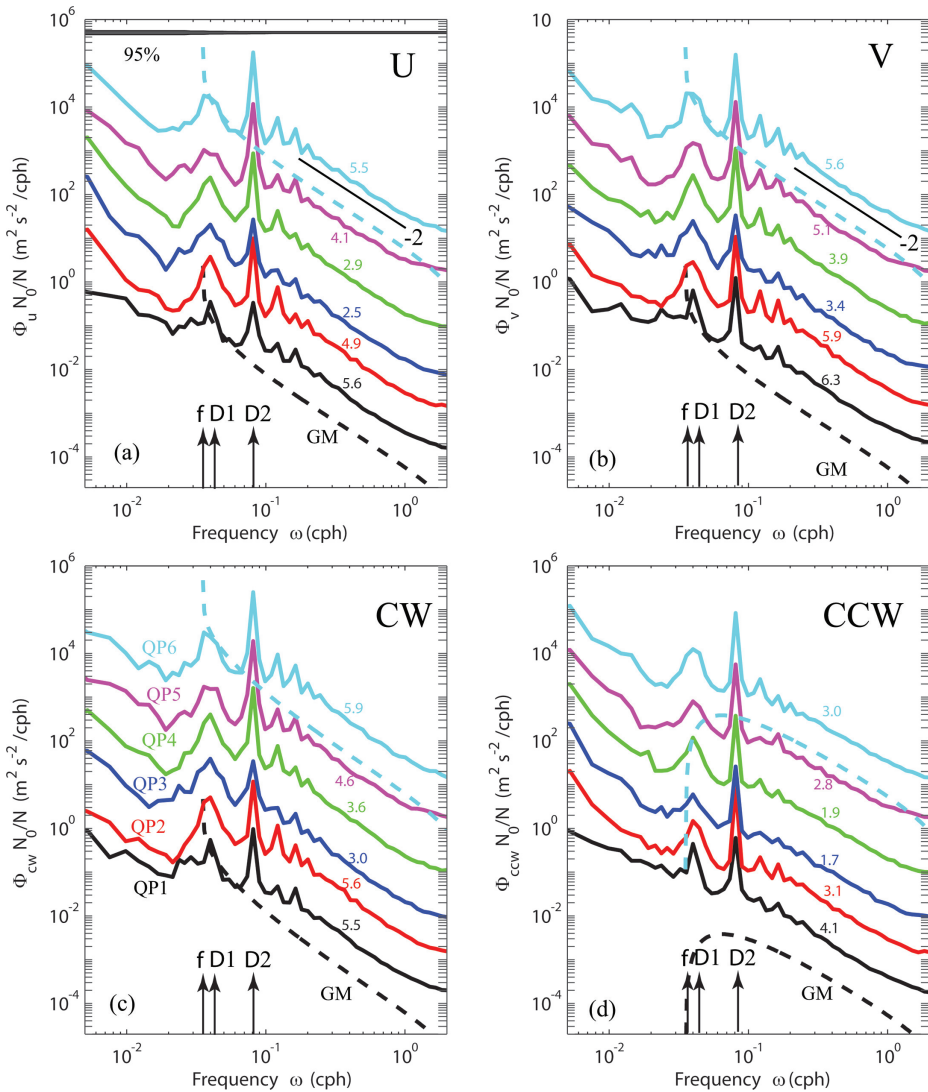
Figure 4. Depth averaged spectra of (a) zonal velocity, (b) meridional velocity, (c) clockwise velocity and (d) counterclockwise velocity on six moorings. For each mooring, spectra are computed at depths between 50 and 500 m, WKB scaled, and vertically averaged. Colors of curves represent spectra at different mooring sites (indicated in panel c). Spectral levels at QP2, QP3, QP4, QP5 and QP6 are multiplied by 10, 10^2, 10^3, 10^4 and 10^5 for a better comparison. Black and cyan dashed curves represent GM spectra at QP1 and QP6, for comparison with observed spectra. Color numbers represent the ratio of observed and GM variance integrated between 0.2 cph and 1 cph, within the internal wave continuum. Inertial (f), diurnal (D1) and semidiurnal (D2) frequencies are labeled. Shading in panel (a) represents the 95% confidence interval of spectra.
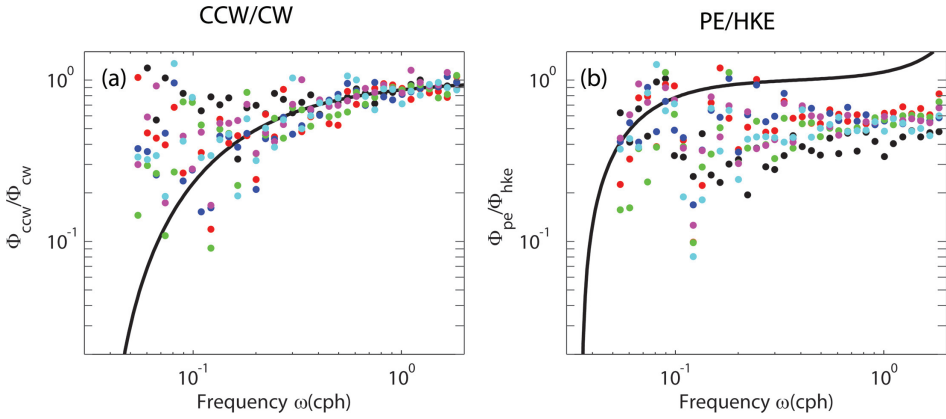
Figure 5. Consistency test for random linear internal waves using mooring measurements. (a) Observed ratio between counterclockwise and clockwise velocity frequency spectra (color dots), WKB normalized and vertically averaged, compared with the theoretical ratio for linear internal waves (black curve). (b) Observed ratio between potential energy and horizontal kinetic energy (color dots) compared with the theoretical ratio for random linear internal waves (black curve). Colors of dots correspond to the moorings QP1–6 (see Fig. 4).

zonal, meridional and clockwise velocities are 8 to 12 times larger than the GM at moorings QP1, 2, 5 and 6, and 5 to 8 times larger at QP3 and 4. Because our observations represent internal waves near the generation site of semidiurnal internal tides, strong energy in the internal wave continuum via wave–wave interaction is expected. Inertial waves are also the source of internal waves. During Aug. 6–8, 2009, Typhoon Morakat passed south and west of our moorings (Gawarkiewicz et al., 2011). Strong inertial waves generated by Morakat might also contribute to the observed high internal wave energy compared to the GM spectral model.

Clockwise velocity spectra Φ_{cw} are stronger than counterclockwise velocity spectra Φ_{ccw} as expected for linear internal waves. For a superposition of random linear internal waves, the ratio between counterclockwise and clockwise velocity spectra follows $\frac{\Phi_{ccw}}{\Phi_{cw}} = \frac{(\omega-f)^2}{(\omega+f)^2}$. This consistency relation is derived using the dispersion and polarization relations (Fofonoff, 1969; Müller et al., 1978). It is also valid for vertical standing waves (Müller et al., 1978). Observed rotary spectra are WKB normalized and averaged over depth. Ratios of WKB normalized and vertically averaged rotary spectra at all mooring sites are shown in Figure 5. They are consistent with linear internal waves at frequencies beyond 0.2 cph, i.e., beyond frequencies of the semidiurnal tide and tidal harmonics. We do not expect that internal waves are linear at semidiurnal tidal frequencies or tidal harmonics.

Potential energy spectra are computed as $\Phi_{PE}(\omega) = 1/2N^2\Phi_\eta(\omega)$, where $\Phi_\eta(\omega)$ is the vertical displacement spectrum. Vertical displacement at any depth is computed as $\eta(t,z) = -(T(t,z) - \overline{T(z)})/\partial_z\overline{T(z)}$, where $\overline{T(z)}$ is the low-pass filtered temperature at time scales greater than 72 hours. The potential energy spectra are WKB normalized,
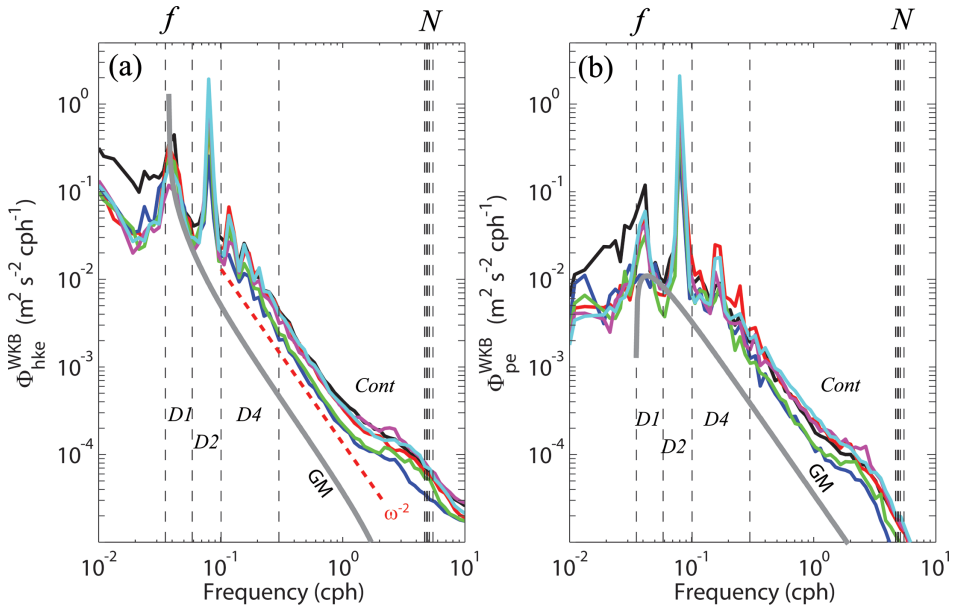
Figure 6. Depth averaged and WKB adjusted (a) horizontal kinetic energy spectra and (b) potential energy spectra at QP1 (black), QP2 (red), QP3 (blue), QP4 (green), QP5 (magenta) and QP6 (cyan). The inertial frequency (f) and buoyancy frequency (N) are marked. We divide internal wave energy density into distinct frequency bands: diurnal tidal band (D1), semidiurnal tidal band (D2), higher tidal harmonic band (D4) and internal wave continuum (Cont). Energy contents of different frequency bands are summarized in Table 2. The gray curves represent GM spectra.

$\Phi_{PE}(\omega)N_0/N(z)$, and averaged over depths to yield one averaged WKB spectrum for each mooring (Fig. 6).

WKB normalized and depth averaged horizontal kinetic energy and potential energy spectra are divided into four internal wave frequency bands: inertial to diurnal tidal band (D1), semidiurnal tidal band (D2), tidal harmonics (D4), and internal wave continuum (Cont) (Fig. 6). The total energy, the sum of horizontal kinetic and potential energy, is integrated in these frequency bands (Table 2). The total energy integrated over the entire internal wave frequency band varies from the weakest, 16.5 J m^{-3} at QP3, to the strongest, 44.3 J m^{-3} at QP2. Compared to the total energy, 2.95 J m^{-3} in GM, internal waves on the ECS continental slope are 5.7–15.3 times the GM. The semidiurnal tidal energy contributes more than 50% of internal wave energy, varying from 9.2 J m^{-3} at QP3 to 32.0 J m^{-3} at QP6. In the internal wave continuum, the total energy varies from 1.2 J m^{-3} at QP3 to 2.7 J m^{-3} at QP1, i.e., 6.2–13.3 times the GM value of 0.2 J m^{-3}. Both the energy at the semidiurnal tidal band and energy within the internal wave continuum increase from QP3, QP5, QP4, QP2, to QP6, suggesting energy transfer from semidiurnal tides to the internal wave continuum. Similarly, the energy in D4 fluctuates in unison with that in D2, suggesting

Table 2. Depth-averaged, WKB-scaled total energy (horizontal kinetic energy + potential energy), in various internal wave frequency bands in units of J m^{-3}. D1 represents the inertial and diurnal frequency band, D2 the semidiurnal band and D4 the tidal harmonic band. Numbers in the parentheses in the last two columns indicate the ratios to those of GM values. The total energy within the internal wave continuum and in the entire internal wave band of the GM spectrum is 0.2 J m^{-3} and 2.95 J m^{-3}, respectively.

Mooring	D1 (0.035– 0.058 cph)	D2 (0.058– 0.101 cph)	D4 (0.101– 0.3 cph)	Internal Wave Continuum (0.3 cph – N) (GM = 0.2 J m^{-3})	Total Internal Wave Band (GM = 2.95 J m^{-3})
QP1	3.3	16.3	4.3	2.7 (13.3 GM)	27.5 (9.5 GM)
QP2	4.5	31.8	5.1	2.2 (11.2)	44.3 (15.3)
QP3	3.2	9.2	2.3	1.2 (6.2)	16.5 (5.7)
QP4	2.9	22.5	3.3	1.5 (7.3)	30.7 (10.6)
QP5	2.7	18.2	3.0	2.2 (11.2)	26.7 (9.2)
QP6	3.5	32.0	5.3	2.6 (13.0)	44.1 (15.2)

wave–wave interaction. The energy in the diurnal tidal frequency band is 10–34% that in the semidiurnal frequency band. This is in contrast to the observations on the ECS continental shelf where the diurnal internal tidal energy is stronger than the semidiurnal internal tidal energy (Duda et al., 2013).

For a superposition of random linear internal waves, the ratio between the potential energy and horizontal kinetic energy frequency spectra is $\frac{\Phi_{PE}(\omega)}{\Phi_{HKE}(\omega)} = \frac{N^2}{N^2-\omega^2}\frac{\omega^2-f^2}{\omega^2+f^2}$ (Fofonoff, 1969 and Müller et al., 1978). We find that the observed ratio in the internal wave continuum is about one-half of the prediction from the above consistency relation. Similar energy disparity has been reported from IWEX observations (Müller et al., 1978) and in Fofonoff's study (Fofonoff, 1969).

For a vertical standing linear internal wave the ratio of PE to HKE frequency spectra varies with depth, i.e., $\gamma^*_{PE/HKE} = \frac{\Phi_{PE}(\omega)}{\Phi_{HKE}(\omega)} = \frac{N^2}{N^2-\omega^2}\frac{\omega^2-f^2}{\omega^2+f^2}\frac{\sin^2(mz)}{\cos^2(mz)}$, where m is the vertical wavenumber and z is depth (Appendix B). For first-mode internal waves in the ocean of a constant N, $m = \pi/H$, where H is the water depth. The vertical displacement, thereby the potential energy, vanishes at the sea surface and bottom. The horizontal velocity vanishes at the mid-depth. Therefore, the ratio PE/HKE is zero at the surface and bottom, and becomes infinity at the mid-depth. The observed energy disparity suggests any of a combination of processes including nonlinear internal waves, phase-locked linear internal waves and vortical motions (Müller, 1988) in the internal wave continuum.

4. Generation sites of semidiurnal internal tides

Internal tides are often generated on the continental shelf break when strong barotropic tidal currents flow onto the continental shelf. The vertical motion associated with the

shoaling barotropic tide uplifts the stratified water at tidal frequencies and generates internal tides. The OSU TPXO predicts a strong semidiurnal barotropic tidal current flowing nearly perpendicular to the ECS shelf break (Fig. 7). On the continental shelf, <200 m water depth, the major axis of the barotropic semidiurnal tidal current ellipse is nearly aligned in the NW–SE direction with an amplitude as large as 0.6 m s^{-1}. The semidiurnal barotropic tidal current lessens dramatically on the continental slope, ∼0.2 m s^{-1} at mooring QP2 and ∼0.3 m s^{-1} at moorings QP5 and QP6.

Bains (1982) suggested that one of the most important parameters in determining the generation of internal tides on the continental shelf is the ratio between the bottom slope and the slope of internal wave characteristics, hereafter referred to as criticality, $\Lambda = \gamma/\alpha$, where $\gamma = \nabla h$ is the bottom slope and $\alpha = (\omega^2 - f^2)^{1/2}/(N^2 - W^2)^{1/2}$ is the slope of internal wave characteristics. Bains suggested that the generation of the internal tides is the strongest when the criticality is approximately one, where internal wave energy is also enhanced. A criticality less than one is called subcritical and greater than one is called supercritical. Internal waves propagate up the subcritical slopes and reflect on supercritical slopes.

We compute internal wave characteristic slopes using the mean vertical profile of stratification observations from EM-APEX floats. The vertical profile of stratification computed from mooring measurements agrees with that from EM-APEX floats (Fig. 7b). The peak N is at about 50-m depth, which is nearly twice that of the average from historical CTD data (Taiwanese Ocean Data Center). The observed stronger stratification may be due to the effect of Typhoon Morakat, which produced an abnormally fresh upper ocean through precipitation and river runoff (Jan et al., 2013; Gawarkiewicz et al., 2011).

The region with the criticality Λ between 0.5 and 2 for semidiurnal internal tides, near our mooring sites, is shaded in Figures 7 and 8. The primary generation sites of semidiurnal internal tides on the ECS are identified as (1) along the shelf break north of the head of NMH Canyon, (2) a broad area west of moorings QP2 and QP6 between the 300 and 500 m isobaths, and (3) a narrow area between the 800 and 1,000 m isobaths south of the QP2 mooring. The strongest generation site for the semidiurnal internal tide is expected at (2) because of its broad area and strong barotropic tide.

The largest region of criticality Λ (Fig. 8) corresponds to the strongest generation site (2), centered at 25.4°N and 122.5°E, a ∼150 × 150-km area. QP6 is the closest to this generation site, QP2 and QP5 next, and QP3 and QP4 the farthest away. This might explain the strongest internal tidal energy observed at QP2 and QP6 and the weakest at QP3 (Table 2).

Near the generation site, internal tides may appear as a tidal beam, with superposition of low and high vertical modes (Garrett and Kunze, 2007). We illustrate possible internal tidal beams propagating past mooring QP2 along the magenta line in Figure 8. First we assume the semidiurnal internal tidal beam is generated at the continental shelf break and propagates along its ray path (Fig. 9). One upward tidal beam propagates shoreward onto the continental shelf, and an upward beam and a downward tidal beam propagate seaward. The upward seaward beam reflects off the sea surface ∼15 km east of the shelf break
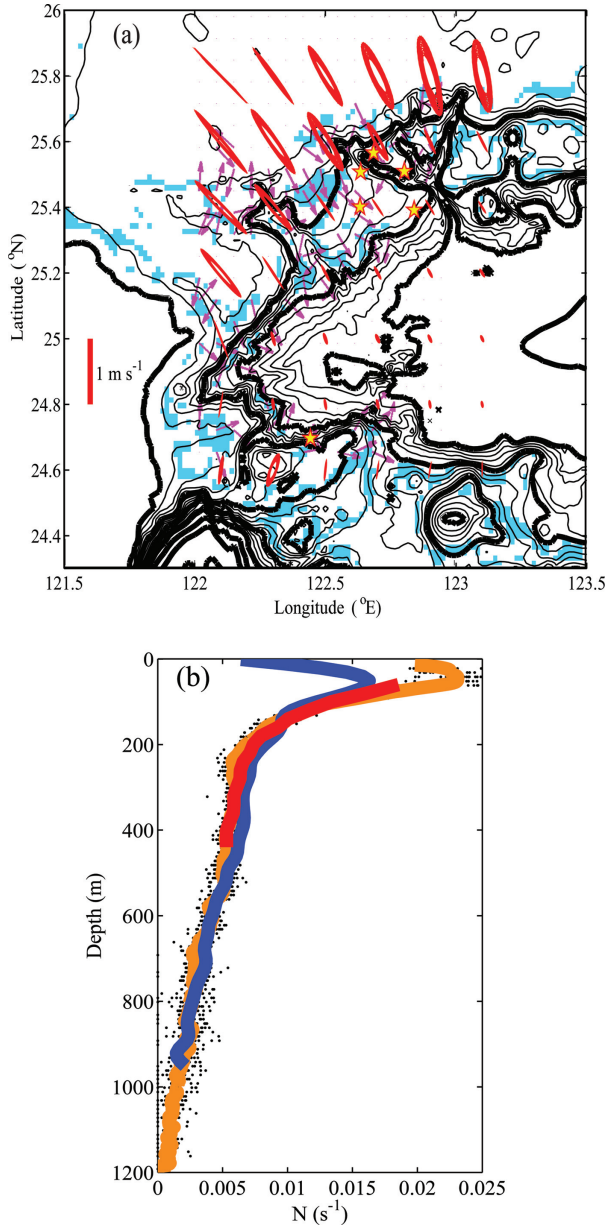
Figure 7. (a) Bathymetry map off NE Taiwan, critical slope (cyan shading) where the ratio between bottom slope and internal wave characteristic slope is between 0.5 and 2, barotropic tidal current ellipses (red ellipses) and mooring locations (yellow stars) and (b) averages of vertical profiles of stratification computed from historical CTD data provided by Taiwanese Ocean Data Center (blue curve), from EM-APEX float measurements (orange curve) and from moorings on East China Sea continental slope (red curve). Black dots are data from EM-APEX floats. On panel (a), magenta vectors within cyan shading area represent the direction of the bathymetry gradient. The reference 1 m s^{-1} velocity scale for barotropic tidal current is shown in (a).
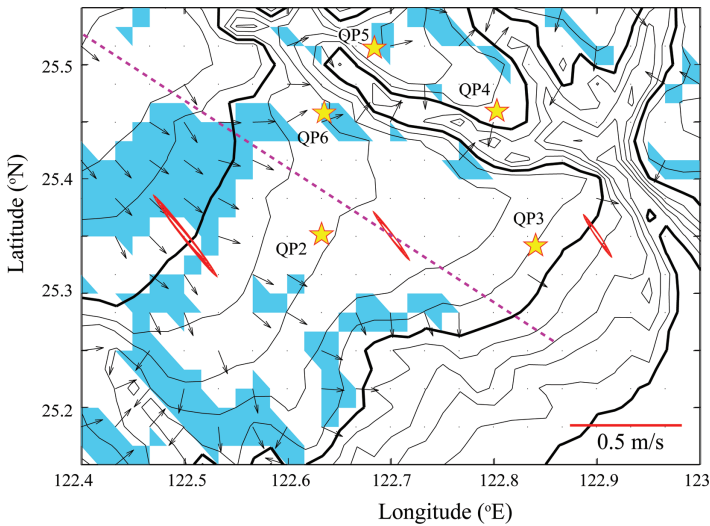
Figure 8. Detail from Figure 7 showing the critical slope regions (cyan shading), slope gradient (arrows), and locations of five moorings. Three red ellipses are barotropic tidal current ellipses computed from TPXO. The magenta dashed line indicates the section shown in Figure 9. The horizontal red line shows the velocity scale of 0.5 m s^{-1}.

and propagates downward passing the QP2 mooring centering at 70 m depth and into the deep ocean. The downward seaward beam, emanating from the shelf break, reflects off the critical slope, site B in Figure 9, is amplified, and propagates upward passing mooring QP2 at 400 m depth. Another tidal beam emanating from the upper critical slope, site A (Fig. 9), propagates upward passing the QP2 mooring at about 80 m depth. Tidal beams generated within the critical slope zone, between sites A and B in Figure 9, propagate upward passing the QP2 mooring between 80 and 400 m depth.

The temporal average of horizontal kinetic energy in the semidiurnal tidal frequency band at QP2 shows strong energy in the upper 100 m and below 400 m depth, and weak energy in the mid-depths. This agrees with the ray tracing results for internal tides generated at the shelf break. However, this vertical structure can also be explained by the first-mode internal tides. The same ray tracing analysis applied to the other mooring sites suggests similarly that both upward and downward tidal beams arrive at the sites.

A snapshot of horizontal kinetic energy from the Princeton Ocean Model (POM) (Blumberg and Mellor, 1987) forced by the M_2 tide (described in Section 7) is shown in Figure 9b. A downward internal tidal beam is generated on the shelf break propagating seaward. Another internal tidal beam is generated on the critical slope, between sites A and B in Figure 9a, propagating upward passing the QP2 mooring between 50 and 300 m depth. Numerical model results are qualitatively in agreement with those from the critical slope and ray tracing analyses.
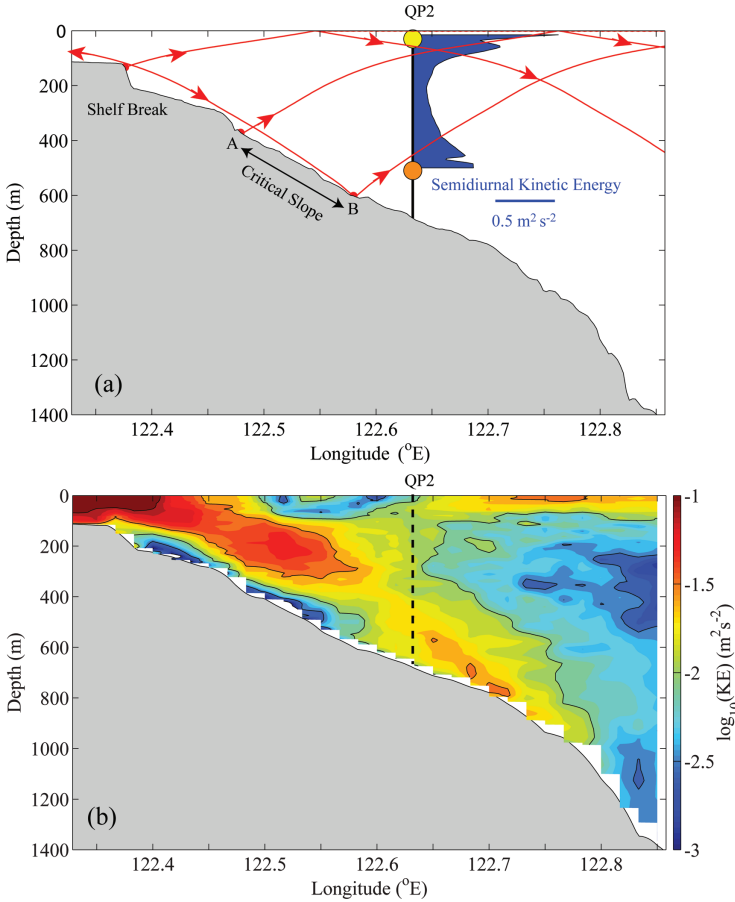
Figure 9. (a) Illustration of characteristics of internal tides generated at the shelf break and bouncing off the critical sloping bottom and off the sea surface, and generated at the critical slope (red curves) along the section shown as the magenta dashed line in Figure 8. They are computed using stratification observed from EM-APEX floats. The blue shading shows the semidiurnal tidal kinetic energy observed at mooring QP2. The brown and yellow dots represent the two subsurface floats of the mooring. The scale of kinetic energy of $0.5\ \mathrm{m^2 s^{-2}}$ is shown. (b) A snapshot of model results of the horizontal kinetic energy of M_2 semidiurnal tide along the same section at day 5.25 of the model run. These results are from the model run M2a described in Section 7 (Fig. 17). The vertical dashed line indicates the location of mooring QP2.

5. High-wavenumber internal tides and spatially coherent shear layers

a. Observed vertical propagation of internal tides

A two-day time series of semidiurnal band-pass filtered horizontal velocity and vertical shear at mooring QP2, shows zonal velocity upward phase propagation, implying a
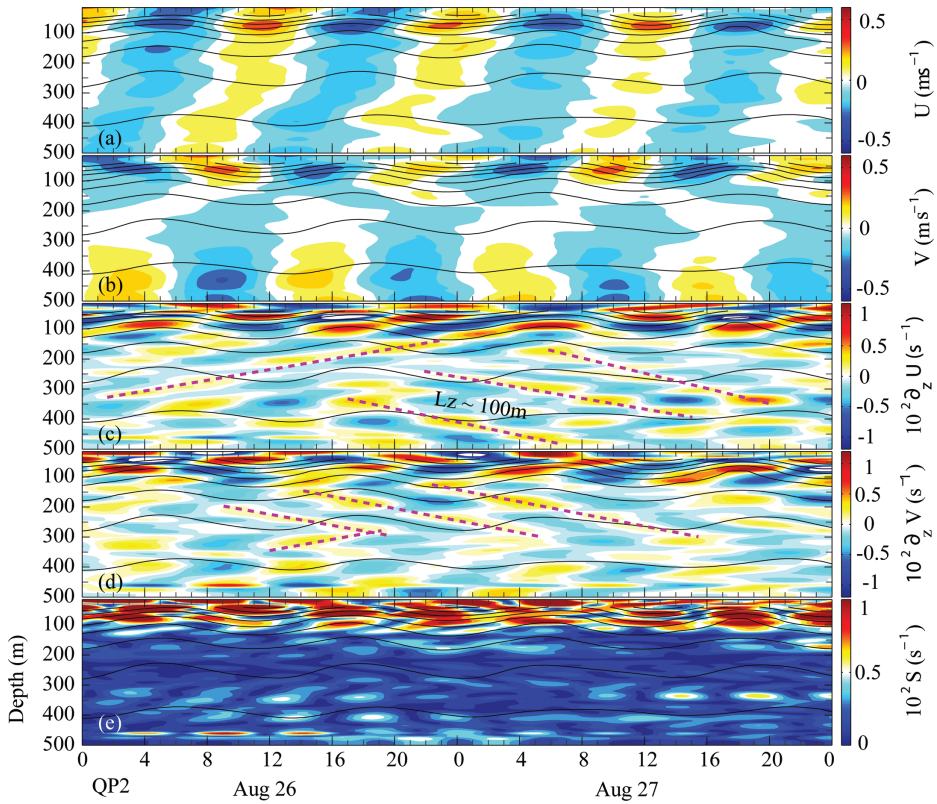
Figure 10. Semidiurnal bandpass-filtered (a) zonal velocity, (b) meridional velocity, (c) vertical shear of zonal velocity, (d) vertical shear of meridional velocity and (e) the magnitude of total vertical shear. Black contour curves represent isopycnals. Magenta dashed lines illustrate some constant phase lines.

downward energy propagation (Fig. 10a). The meridional current, however, does not show vertical phase propagation, but rather a vertical standing mode structure (Fig. 10b). The disparity of the vertical structure of zonal and meridional velocities illustrates the complexity of internal tides on the ECS slope, where multiple generation sites are present and the internal tide propagation is strongly modulated by the abrupt change of topography over the continental slope and submarine canyons. We postulate that the downward propagation of the zonal energy is a result of internal tidal beams propagating seaward from the shelf break and the standing modal structure of the meridional energy is a combination of upward and downward energy propagation, probably from multiple sources.

Small vertical scale velocity fluctuations are embedded in the large vertical scale fluctuations of zonal and meridional velocity, e.g., Aug. 27, 0200–0900Z (Fig. 10a). They are

apparent in vertical shear (Fig. 10c and 10d). In the upper 100 m, the vertical shear shows mostly upward phase propagation (downward energy propagation), although sometimes it becomes less apparent, e.g., during Aug. 26, 0400–1200Z. At depths greater than 100 m, both upward and downward propagations are present. The small vertical scale internal tide has a dominant scale of $O(100\,\mathrm{m})$. A crude estimate of downward phase propagation is ~ 0.2 cm s^{-1}. The magnitude of the vertical shear of horizontal velocity, $[(\partial_z U)^2 + (\partial_z V)^2]^{1/2}$, is strongest, $O(0.01\,\mathrm{s}^{-1})$, in the upper 100 m. Some patches of strong vertical shear with a vertical scale of ~ 50 m are present between 300 and 500 m depth on Aug. 26.

Shipboard ADCP measurements taken during the QPE experiment reveal that these shear layers are spatially coherent across the continental slope (not shown). Rainville and Pinkel (2004) reported similar high-wavenumber coherent shear layers on the ECS continental slope further downstream of the Kuroshio. They proposed that the coherent shear layers are either inertial waves resulting from the interaction of the Kuroshio with the topography or internal tides. Assuming the turbulence kinetic energy dissipation rate scaled with shear squared (Gregg, 1989), dissipation as high as 30 times the open ocean value is anticipated as a result of the coherent shear layers.

b. Decomposition of upward and downward propagating waves

We decompose the observed velocity into upward and downward propagating waves (Appendix C). Velocity observations are transformed into the vertical wavenumber and frequency Fourier space. Fourier coefficients in the positive vertical wavenumber and positive frequency represent the downward energy propagation waves; those in the negative vertical wavenumber and positive frequency represent the upward energy propagation waves. Separately, they are inversely Fourier transformed back to the depth and time physical spaces.

Decomposition results of observations between Aug. 24 and 27 are illustrated in Figure 11. The observed velocity field is first band-pass filtered at the semidiurnal tidal frequency band, at 6–18-hour period. The semidiurnal tidal velocity is WKB normalized, and the vertical scale is WKB stretched. We further separate the low-wavenumber internal tides (Fig. 11b) from the high-wavenumber internal tides (Fig. 11c) using a low-pass filter at the half-power point of a 300 m vertical stretch scale. High-wavenumber internal tides are decomposed into components of upward and downward energy propagation (Fig. 11d and 11e).

Several distinct features are revealed. Some are common features for the entire experimental period, but some are unique to this particular three-day period. Low-wavenumber internal tides have stronger energy than high-wavenumber internal tides and exhibit predominant upward phase propagation (downward energy propagation) (Fig. 11b). The high-wavenumber internal tide has a complex temporal–spatial pattern (Fig. 11c), consisting of both upward and downward propagating waves (Fig. 11d and 11e). Interestingly, the superposition of upward and downward propagation waves of high-wavenumber internal tides
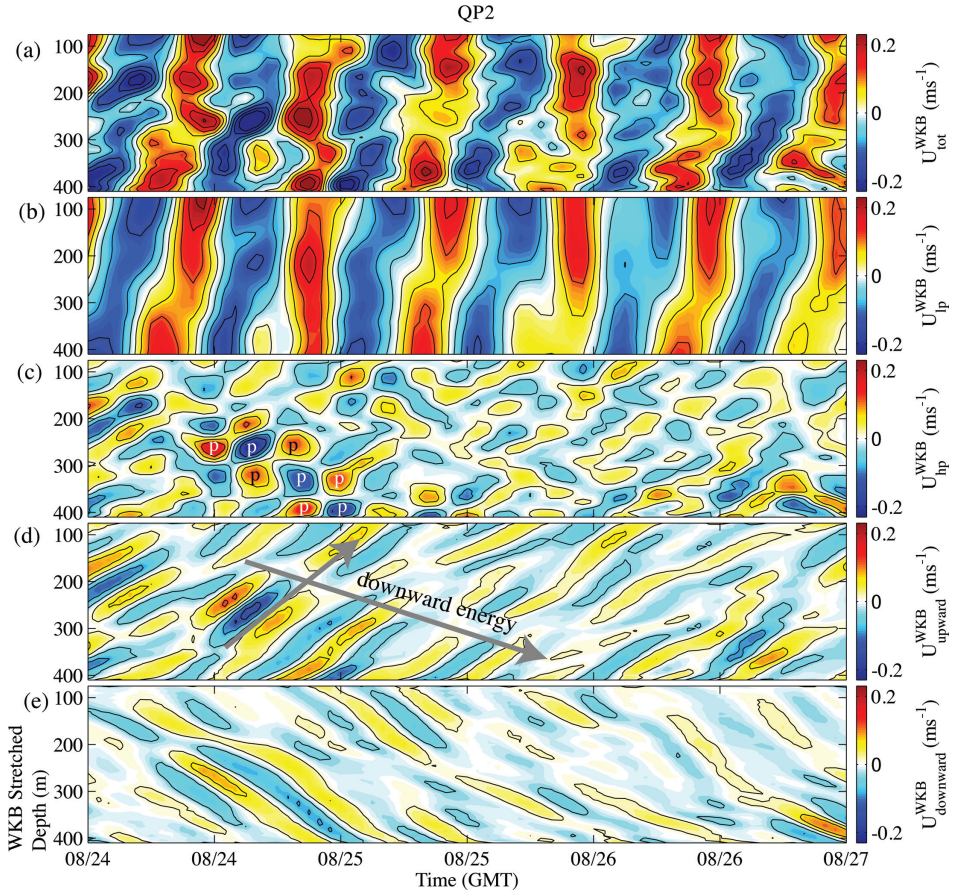
QP2

Figure 11. Decomposition of upward and downward propagation waves at QP2. (a) WKB scaled zonal velocity component band-pass filtered in the semidiurnal tidal period in the WKB stretched vertical coordinate. (b) Zonal velocity low-pass filtered (low wavenumber) with vertical scales greater than 300 m and (c) zonal velocity with vertical scales less than 300 m (high wavenumber). (d) and (e) Decomposition of high vertical wavenumber velocity in (c) into the upward phase propagation and downward phase propagation, respectively. Two gray arrows in (d) represent the downward energy propagation, and the upward phase propagation of internal tidal energy. Patches in (c) labeled 'p' represent the intensification of high vertical wavenumber velocity due to the superposition of upward and downward propagation waves.

results in patches of enhanced energy of ∼50-m scales between Aug. 24 and 25 (labeled 'p' in Fig. 11c).

Between Aug. 24 and 25, a group of waves was observed propagating downward ∼300 m in two days (gray downward arrow in Fig. 11d) corresponding to a vertical group speed of 0.0017 m s^{-1}. For linear internal waves with a hydrostatic approximation, the vertical

energy propagation speed $C_z^g = \frac{\partial \omega}{\partial m} = \frac{N^2}{\omega_{D2}} \frac{k_h^2}{m^3}$, where m is the vertical wavenumber, k_h is the horizontal wavenumber, and ω_{D2} is the frequency of semidiurnal tides, and the horizontal energy propagation speed $C_h^g = \frac{\partial \omega}{\partial k_h} = \frac{N^2}{\omega_{D2}} \frac{k}{m^2}$. Given the averaged N of 4.5 cph and vertical wavenumber of ~ 0.0083 cpm (identified from the vertical wavenumber spectrum, not shown), the horizontal wavenumber magnitude k_h can be computed using the dispersion relation of linear internal waves as $\sim 1.4 \times 10^{-4}$ cpm, a horizontal wavelength of 7.1 km. The vertical energy propagation speed C_z^g is ~ 0.0023 m s^{-1}. The two estimates of vertical energy propagation speed agree within $\sim 30\%$. The horizontal energy propagation speed of high-wavenumber internal tides is 0.14 m s^{-1}. The low-wavenumber internal tides have a vertical scale comparable to the water depth, say 700 m. A crude estimate of the horizontal energy propagation speed is ~ 0.79 m s^{-1}, at least five times greater than that of high-wavenumber internal tides. The horizontal energy propagation speed C_h^g can also be estimated using the eigen speed c_e computed from the eigenmode analysis, i.e., $C_h^g = \frac{\sqrt{\omega^2 - f^2}}{\omega} c_e$ (Alford et al., 2007). The mode-1 eigen speed $c_e = 0.9$ m s^{-1}, and therefore $C_h^g = 0.81$ m s^{-1}. The two estimates are in good agreement.

It takes one-two days for high-wavenumber internal tides to propagate from the shelf break to mooring QP2, ~ 15 km distance, and only a few hours for low-wavenumber internal tides. The spatially coherent shear layers associated with high-wavenumber internal tides propagate at a very low speed and are the prominent feature on the continental slope. Because high-wavenumber internal tides contain strong vertical shear, $O(0.01 \text{ s}^{-1})$, they may play an important role in the shear instability and turbulence mixing on the ECS continental slope.

The vertical distribution of WKB-scaled horizontal kinetic energy of the semidiurnal internal tides at mooring QP2 is averaged over the observational period (Fig. 12). We separate the velocity into the low-wavenumber and high-wavenumber components and decompose into the upward and downward propagation components. For the total and low-wavenumber internal tides, the horizontal kinetic energy is the strongest near the maximum observation depth, ~ 500 m vertical stretched scale, and the weakest at mid-depths. The high-wavenumber internal tide shows a general increase of horizontal kinetic energy with depth. Low-wavenumber internal tides contribute most of the total horizontal kinetic energy. The upward phase propagation (downward energy propagation) wave is generally 1.5 times stronger than the downward phase propagation wave (upward energy propagation) between 120 and 350 m depths. The stronger upward phase propagation is also seen in Figure 10a.

The temporal variation of depth integrated horizontal kinetic energy, within observational depth range, is shown in Figure 13. Both the total and low-wavenumber horizontal kinetic energy are the strongest at mooring QP6 and the weakest at mooring QP3 (Fig. 14b). The high-wavenumber horizontal kinetic energy shows less variability among moorings. All of the total, low-wavenumber, and high-wavenumber horizontal kinetic energy observations exhibit a fortnightly cycle, in close unison with the barotropic tides.
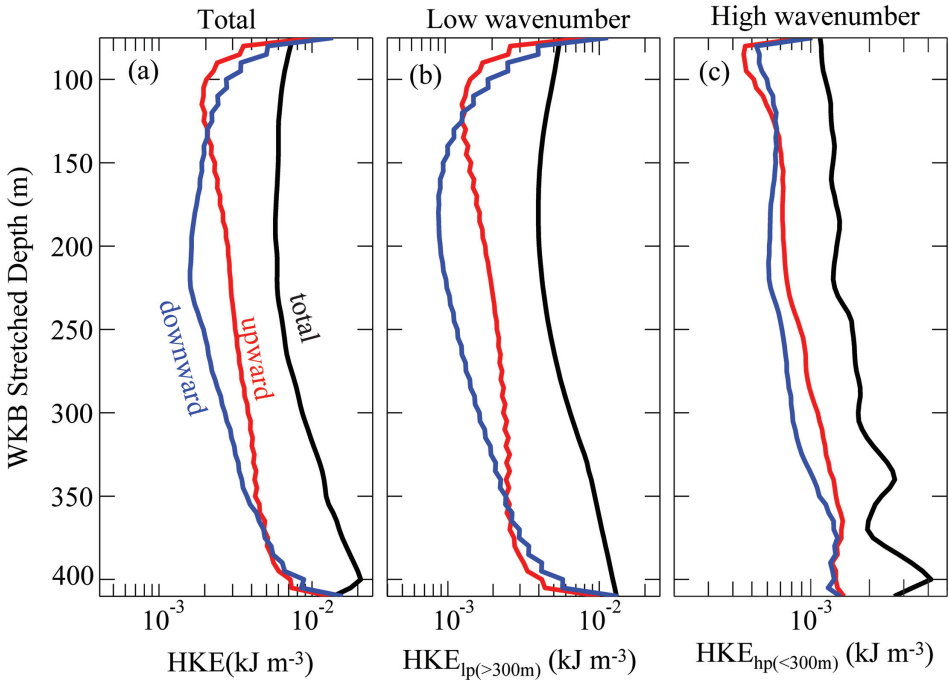
Figure 12. (a) WKB stretched vertical profiles of WKB scaled semidiurnal band-pass filtered hor-
izontal kinetic energy averaged over the observational period (black curve) at QP2, the upward
phase propagation (downward energy propagation) component (red curve), and the downward
phase propagation (upward energy propagation) component (blue), (b) similar to (a) but for waves
at vertical scales greater than 300 m (low wavenumber), (c) similar to (a) but for waves at vertical
scales smaller than 300 m (high wavenumber).

6. Observations of internal tidal energy flux

We compute the semidiurnal internal tidal energy flux following the method described
by Kunze et al. (2002). The application of this method is further investigated by Nash
et al. (2005). The internal tidal energy flux is computed as $F = \langle \vec{u}' p' \rangle$, where $\vec{u}'$ is the
semidiurnal internal tidal velocity vector, p' is the dynamic pressure perturbation associated
with semidiurnal internal tides, and $\langle \bullet \rangle$ represents time averaging. Here, we briefly review
the method discussed in Nash et al. (2005).

The perturbation pressure is computed using the observed density. First, the density
anomaly $\rho'(z, t)$ is estimated as

$$\rho'(z, t) = \rho(z, t) - \bar{\rho}(z),$$

where $\rho(z, t)$ is the measured density and $\bar{\rho}(z)$ is the time averaged density at every depth.
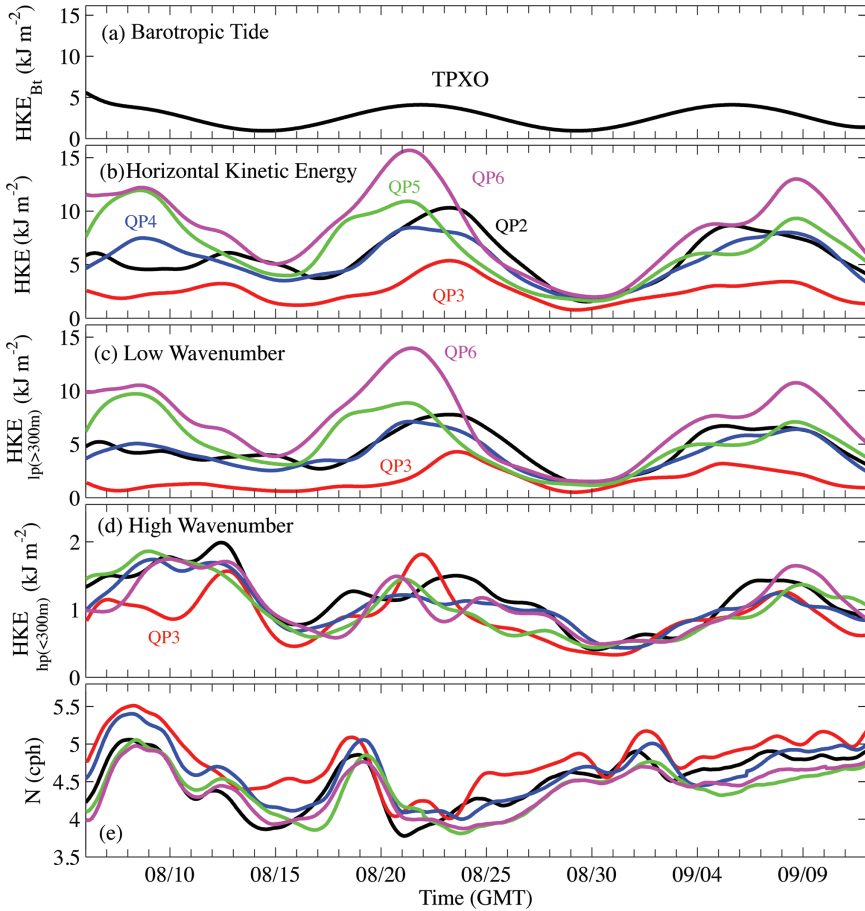
Figure 13. Temporal variations of (a) depth integrated horizontal kinetic energy of semidiurnal barotropic tide computed from TPXO, (b) depth integrated horizontal kinetic energy for semidiurnal internal tides, (c) similar to (b) but for vertical scales greater than 300 m (low wavenumber) and (d) similar to (b) but for vertical scales less than 300 m (high wavenumber). (e) Temporal variations of the depth averaged stratifications.

The perturbation pressure $p'(z, t)$ is computed using the hydrostatic approximation

$$p^*(z, t) = p_{surf}(t) + \int_z^0 \rho'(z', t) g \, dz',$$

$$p'(z, t) = p^*(z, t) - \frac{1}{H} \int_{-H}^0 p^*(z, t) \, dz,$$

where p_{surf} is pressure at the sea surface. This method ensures that the vertical integration of perturbation pressure vanishes.
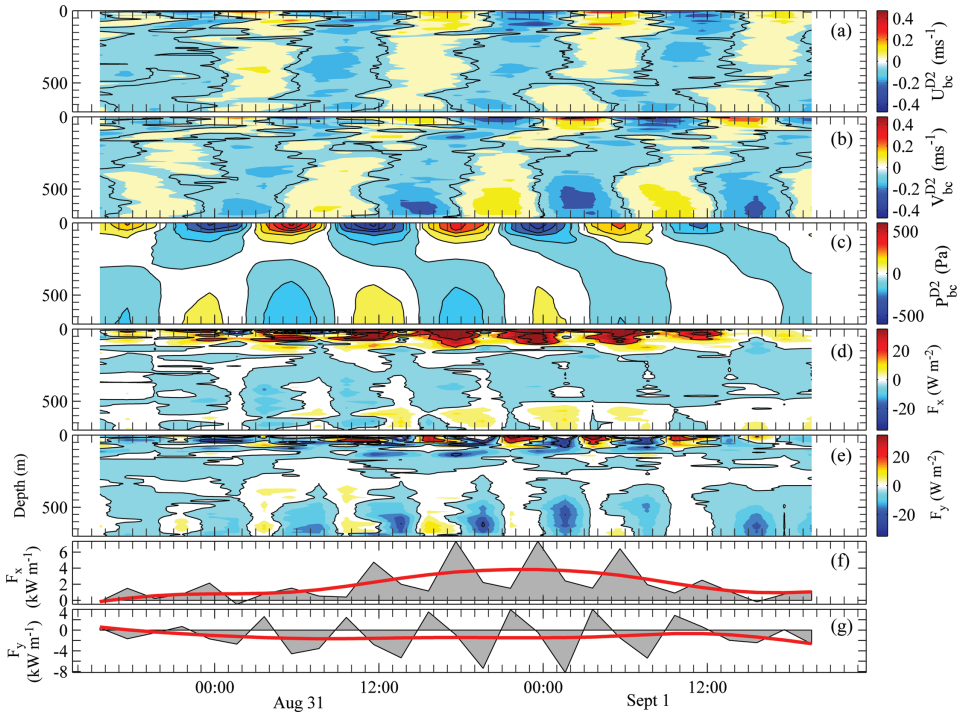
Figure 14. Calculated semidiurnal internal tidal energy flux using measurements from EM-APEX float #4437b in Group D (see Figure 15). (a), (b) and (c) Depth–time contour plots of semidiurnal band-pass filtered baroclinic zonal velocity, meridional velocity and pressure perturbations, respectively. (d) and (e) Depth–time contour plots of the zonal and meridional components of semidiurnal internal tidal energy fluxes, respectively. Gray shadings in (f) and (g) represent the depth integration of zonal and meridional energy fluxes and red curves represent their low-pass filtered energy fluxes at a time scale of 36 hours.

The perturbation velocity is computed as

$$\vec{u}'(z,t) = \vec{u}(z,t) - \overline{\vec{u}}(z) - \overline{\vec{u_0}}(t),$$

where $\vec{u}(z,t)$ is the measured velocity vector, $\overline{\vec{u}}(z)$ is the time averaged velocity at every depth, and $\overline{\vec{u_0}}(t)$ is the barotropic velocity. This computation ensures that the integration of perturbation baroclinic velocity over depth vanishes.

We compute internal tidal energy flux from EM-APEX float observations following the above method. An example using measurements from a two-day EM-APEX float mission is shown in Figure 14. Velocity measurements are band-pass filtered at the semidiurnal band, between 10 and 16 hours and vertical means removed. The semidiurnal internal tidal velocity amplitude is 0.1–0.2 m s^{-1}. Both the velocity and pressure perturbations show
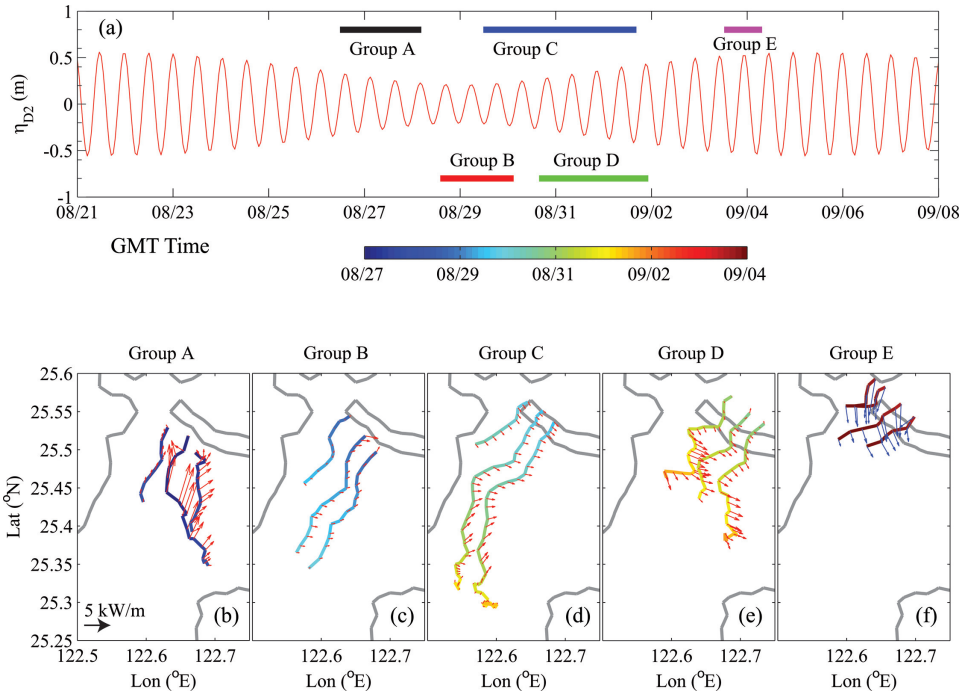
Figure 15. (a) TPXO predicted semidiurnal barotropic tidal elevation, and (b)–(f) the depth integrated semidiurnal internal tidal energy flux (red arrows) along trajectories of EM-APEX floats. EM-APEX floats were deployed in five groups (A–E), each with three or four floats. Color along the trajectories represent the time, corresponding to the horizontal color bar. The reference scale of 5 kW m^{-1} is shown on panel (b). Gray curves in panels (b)–(f) are isobaths of 500 m, 1,000 m and 1,500 m.

a dominant low-mode structure and fluctuate in phase. Their product, the baroclinic tidal energy flux, also reveals a dominant low-mode structure, strong in the upper and bottom layers and weaker at mid-depth. The zonal velocity and pressure are correlated temporally and vertically, leading to a positive tidal energy flux with the maximum values in the upper ocean. The depth integrated zonal energy flux is positive with an average of 2 kW m^{-1} and a maximum of 7 kW m^{-1}. The meridional energy flux has an average of –1.5 kW m^{-1} and a maximum of –8 kW m^{-1}.

EM-APEX floats were deployed in five groups (A–E) of three or four floats each. All floats in each group were deployed within one to two hours. Semidiurnal internal tidal energy fluxes computed from these float measurements reveal strong spatial and temporal variations (Fig. 15). The magnitude of internal tidal energy flux varies in time and shows close correlation with the barotropic tidal forcing, implying that the internal tide in this area is mostly generated locally, instead of remotely. The measurements from Group B reveal the weakest energy flux, corresponding to the weakest barotropic forcing. The energy flux

increases from Group B to group E, following the increase of barotropic tidal forcing. Group A was deployed during the end of spring tide and the internal tidal energy shows the strongest spatial variation in magnitude and direction, 0–10 kW m^{-1}.

The direction of energy flux is complicated; zonal energy flux is mostly positive, i.e., seaward, suggesting generation from the shallow water. The meridional energy flux varies from northward in Group A, to nearly zero in B and C, to southward in D and E. The spatial pattern in group A suggests internal tides generated south of the ECS continental slope and the spatial pattern in Group E suggests internal tides generated north of the head of NMH Canyon. Averaging all estimates of depth integrated internal tidal energy flux, the zonal component is 1.3 ($\pm$1.3) kW m^{-1}, and the meridional component is –0.3 ($\pm$2.5) kW m^{-1}, where the value within the parentheses represents one standard deviation. The standard deviation indicates the temporal and spatial variability of the flux.

Internal tidal energy flux is also computed from mooring measurements. Our velocity and density measurements are limited to the ~50–500 m depth range, missing the upper 50 m and the bottom 200 m for moorings QP1, 2, 5 and 6, and the bottom 400 m for moorings QP3 and 4. EM-APEX float measurements show that the upper ocean and the bottom layer contribute significant amounts of the internal tidal energy flux (see Fig. 14).

Vertical eigenmode analysis is used to estimate the full water column velocity and density profiles using mooring measurements in the 50–500 m depth range. Vertical profiles of stratifications from mooring measurements are low-pass filtered at 36 hours and linearly extrapolated between the surface and 50 m depth, and between 500 m depth and the bottom. The 36-hour period is chosen to compute the background. Vertical eigenmode structures are computed using these slowly varying stratification profiles. Mooring measurements of velocity and density are band-pass filtered at the semidiurnal frequency band, between 10 and 16 hours, and fitted to the barotropic and 1st and 2nd baroclinic eigenmodes. Note that fitting to higher eigenmodes introduces noise into the modal decomposition. The sum of the first and second baroclinic velocity and density vertical profiles is used to compute the internal tidal energy flux. Internal tidal energy fluxes averaged over the entire observational period (Aug. 5–Sept. 12) and over the EM-APEX float observational period (Aug. 26–Sept. 5) are summarized in Table 3.

The internal tidal energy flux is strong during the second and third spring tides at all mooring sites except QP5 (Fig. 16). The average internal tidal energy flux is the strongest, 10.7 kW m^{-1}, at QP4, mostly eastward. Internal tidal energy fluxes at moorings QP2 and QP6 are moderate with similar magnitudes and directions. QP5 has the weakest internal tidal energy flux, 4.1 kW m^{-1} (Table 3). All moorings show positive zonal energy flux, i.e., seaward, supporting the hypothesis that internal tides are generated from the shelf/slope region.

To compare estimates of internal tidal energy flux from moorings with EM-APEX float measurements, we averaged internal tidal energy fluxes over the period of EM-APEX float observations (Table 3). Estimates from mooring observations, 3.0–6.9 kW m^{-1}, significantly exceed those from float measurements. Averaging internal tidal energy fluxes from QP2,

Table 3. Summary of depth integrated semidiurnal internal tidal energy fluxes at mooring sites, in units of kW m^{-1}. F_x, F_y, $|F|$, and F_{dir} represent the zonal and meridional component of energy flux, magnitude, and direction, respectively. Superscripts ^{obs}, ^{run1} and ^{run2} represent observations, model run#1 (M2a), and model run#2 (M2), respectively. Subscripts $_{All}$ and $_{EM}$ represent averages over the entire mooring observational period (Aug. 6–Sept. 16) and over the EM-APEX observational period (Aug. 26–Sept. 4), respectively. Bold highlights the maximum semidiurnal internal tidal energy flux and underlines highlight the minimum semidiurnal internal tidal energy flux on the ECS continental slope.

Mooring	$(F_x^{obs}, F_y^{obs})\|_{All}$ $(\|F^{obs}\|, F_{dir}^{obs})\|_{All}$	$(F_x^{obs}, F_y^{obs})\|_{EM}$ $(\|F^{obs}\|, F_{dir}^{obs})\|_{EM}$	(F_x^{run1}, F_y^{run1}) $(\|F^{run1}\|, F_{dir}^{run1})$	(F_x^{run2}, F_y^{run2}) $(\|F^{run2}\|, F_{dir}^{run2})$
QP1	(3.0, −3.8)	(1.9, −2.1)	(0.2, −0.1)	(1.9, −3.2)
	(4.8, −51)	(2.8, −48)	(0.2, −16)	(3.7, −59)
QP2	(6.5, 0.4)	(4.8, −1.1)	(2.8, −3.2)	(2.6, −2.1)
	(6.5, 4)	(4.9, −13)	(4.2, −49)	(3.4, −39)
QP3	(3.8, −4.6)	(3.3, −4.7)	(2.5, −0.5)	(1.0, −1.1)
	(6.0, −50)	(5.7, −55)	(2.5, −12)	(1.5, −48)
QP4	(10.7. −0.1)	(6.9, −0.2)	(4.2, −5.8)	(1.2, −6.2)
	(10.7, 0)	**(6.9,−2)**	**(7.2, −54)**	**(6.4, −79)**
QP5	(4.1, −0.3)	(2.9, 0.7)	(−0.1, −3.7)	(−0.8, −4.2)
	(4.1, −4)	(3.0, 14)	(3.7, −92)	(4.3, −100)
QP6	(5.6, 3.2)	(3.4, 1.6)	(2.4, 1.6)	(0.5, −0.9)
	(6.5, 30)	(3.8, 26)	(2.9, 33)	(1.0, −61)

QP5, and QP6, closer to the trajectories of EM-APEX floats, yields a zonal flux of 3.7 kW m^{-1} and a meridional flux of 0.4 kW m^{-1}, larger than those from EM-APEX float measurements $F_x = 1.3 \ (\pm 1.3) \ \text{kW m}^{-1}$ and $F_y = -0.3 \ (\pm 2.5) \ \text{kW m}^{-1}$. We attribute the discrepancy to the combination of strong spatial variation (Fig. 15) and sampling bias, i.e., a mooring representing point measurements and floats representing space–time mixed measurements. The discrepancy could also be due to errors in estimates of internal tidal energy fluxes from mooring measurements that invoke vertical eigenmode projection to compensate for missing measurements beyond the depth range of the mooring observations. Despite the difference in magnitude, both estimates of internal tidal energy flux from EM-APEX float and mooring measurements show positive zonal (seaward) internal tidal energy flux and stronger zonal than meridional flux.

7. POM internal tidal model in the ECS

The POM (Blumberg and Mellor, 1987) is used to simulate internal tides in the ECS. It is a nonlinear, primitive equation model with Boussinesq and hydrostatic approximations. The vertical axis is transformed to the $\sigma-$ coordinate by $\sigma = (z - \eta)/(H + \eta)$, where z is positive upward with the origin placed at the mean sea level, η is the sea level fluctuation, and H is the mean water depth. The model can resolve weakly nonlinear internal tides
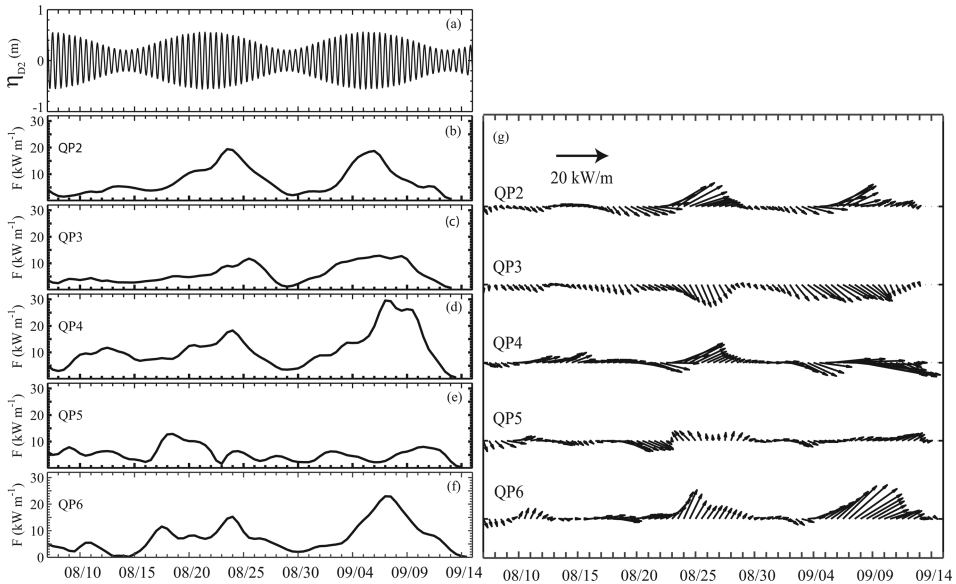
Figure 16. (a) Barotropic semidiurnal tidal elevation computed from TPXO. (b)–(f) Magnitudes of depth integrated semidiurnal internal tidal energy flux at mooring sites on the continental slope. (g) Vectors of depth integrated semidiurnal internal tidal energy fluxes.

that the non-hydrostatic dispersion may neglect (Niwa and Hibiya, 2001; Jan et al., 2008). However, the momentum dissipation and conversion through unresolved non-hydrostatic processes, and the energy transformation from baroclinic tides to nonlinear internal waves are represented by an artificial linear damping term in the horizontal momentum equation. The formula of the damping term is $-r(\vec{u}(z) - \vec{U})$, where $\vec{u}$ is the horizontal velocity vector in the Cartesian coordinate, $\vec{U}$ represents the depth average of $\vec{u}$, and r is an artificial damping coefficient. The damping coefficient $r (=1\ \mathrm{d}^{-1})$ was determined by optimizing the magnitude of baroclinic energy flux derived from the model runs with that from observations. The coefficient is five times greater than that used by Niwa and Hibiya (2001) and Jan et al. (2009), suggesting that a more efficient energy conversion from internal tides to nonlinear internal waves exists in this region than in the open ocean.

The model domain is bounded by 23.33°N and 27°N and 117°E and 124°E (Fig. 1a). The horizontal grid spacing is 1°/60 (~1.85 km), yielding 421 and 281 grids in the x and y directions, respectively. The topography for the canyons off northeastern Taiwan is resolved adequately. Fifty uneven layers are in the vertical σ–coordinate with $\Delta\sigma = 0.002$ from $k = 1$ to 7, $\Delta\sigma = 0.004$ from $k = 8$ to 13, 0.008 from $k = 14$ to 19, $\Delta\sigma = 0.016$ from $k = 20$ to 23, and 0.032 for the other layers (k is an index of the vertical layer from the surface to the bottom). The model uses a 500 m horizontal resolution bathymetry archive provided by the Ocean Data Bank of Taiwan's National Science Council.
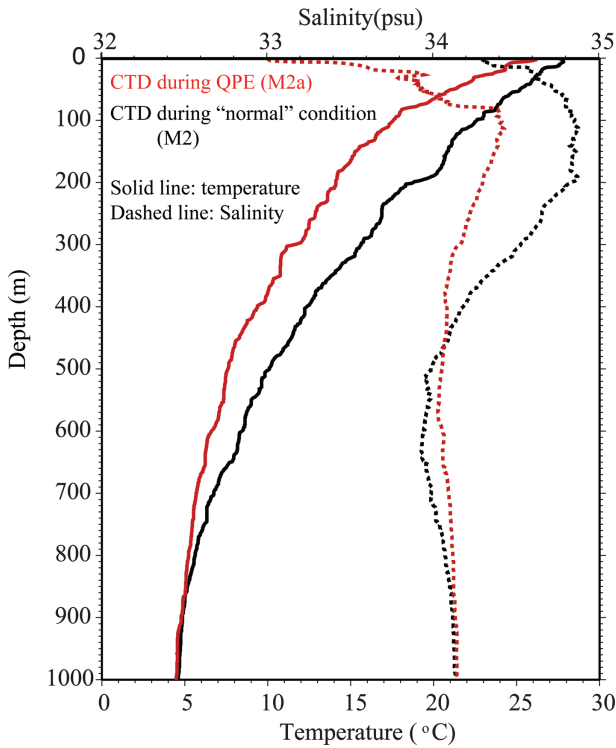
Figure 17. Initial temperature (solid) and salinity (dashed) profiles used in the model. Red represents the CTD data collected ∼1 week after Typhoon Morakot and black represents the CTD data collected during "normal" oceanic conditions near the Okinawa Ridge.

The CTD data obtained at 122.75°E and 25.25°N during Aug. 13–17, 2009 were used as the initial (T, S) fields (Fig. 17) for the entire domain. The low salinity (<34) in the upper 50 m layer was caused by the fresh water pulse brought by Typhoon Morakot (Jan et al., 2013). For comparison, other (T, S) profiles collected at 123.7°E and 25.3°N, farther offshore, during "normal" conditions were used as the initial fields in the model (Fig. 17). Initial (T, S) fields are uniform over the entire model domain. The run with the "normal" (T, S) profile is termed M2 and the run with the post-typhoon (T, S) profile is termed M2a.

The model was driven by the prescribed tidal sea levels at the open boundaries. The tidal sea levels were composed by the harmonic constants that are compiled in a database, TWTIDE08 (Hu et al., 2010). Because M_2 and K_1 are the primary semidiurnal and diurnal constituents, respectively, in the study area (Hu et al., 2010), the internal tide properties of these two constituents are investigated. At the open ocean boundaries, the forced radiation scheme of Blumberg and Kantha (1985) was used for sea level and depth-averaged velocity and the flow relaxation scheme of Martinsen and Engedahl (1987) was applied to three-dimension velocities, temperature and salinity. For the momentum equation, the horizontal
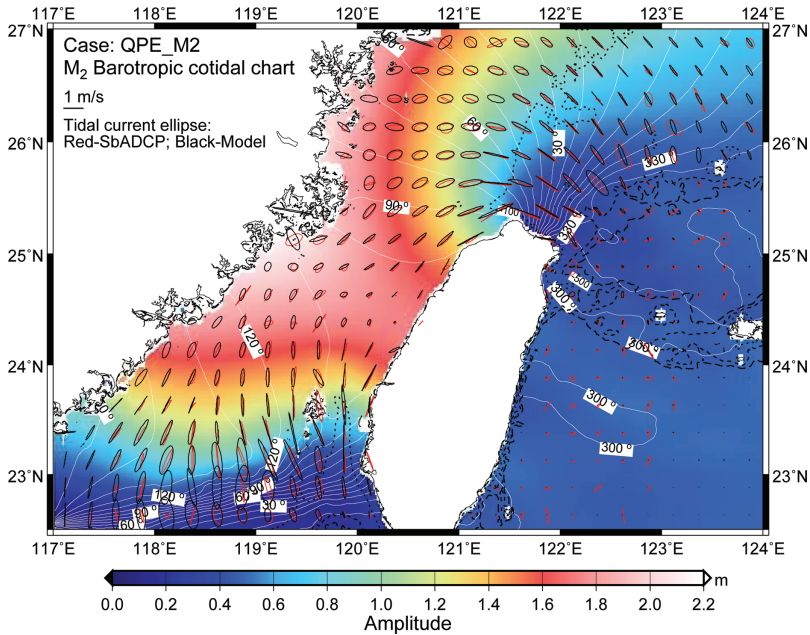
Figure 18. Barotropic co-tidal chart and tidal current ellipses for the simulated M_2 tide. The color codes represent the amplitude and the white lines represent the phase (in degree) of the simulated tides. The red tidal current ellipses are derived from historical shipboard ADCP data (1991–2009) and the black ones are from model results. The short and long dashed lines indicate 100 m and 1,000 m isobaths, respectively.

viscosity and diffusivity were computed according to the formula described in Smagorinsky (1963). The vertical viscosity and diffusivity were determined by a level 2.5 turbulence-closure scheme (Mellor and Yamada, 1982). A quadratic stress law was applied as the bottom boundary condition. To avoid the undesirable drifting of background stratification in time, the horizontal and vertical diffusion of temperature were set to zero. Only the advection effect modulates the (T, S) fields of the model. Also, there was no surface heat flux or salt flux in the model simulation.

Each model run, forced by an individual tidal constituent, lasted for seven days. The modeled flow field reached a cyclic-equilibrium state after approximately three days of integration. The hourly model results during days six and seven were stored for the estimate of the conversion rate of barotropic to baroclinic energy and the baroclinic energy flux.

The tidal sea level and current of the simulated barotropic tides are validated with the harmonic constants of TWTIDE08 and tidal current ellipses derived from the shipboard ADCP data collected in 1991 and 2009. Figure 18 shows the barotropic co-tidal chart (amplitude and phase) and tidal current ellipses for the simulated M_2 tide. The domain averaged, root-mean-square difference between TWTIDE08 and the simulated tidal sea

levels is less than 0.05 m. The simulated barotropic tidal currents of the M_2 tide are comparable to those derived from the historical shipboard ADCP data and to the TPXO results (Fig. 7). The major axes of the M_2 barotropic tidal currents are essentially perpendicular to the continental shelf edge/break off northeastern Taiwan, with a current velocity amplitude of approximately 0.5 m s^{-1} (see also Fig. 7). The barotropic tidal currents are weak in deep waters compared to those on the continental shelf and the topographic ridges. The difference is insignificant between the simulated barotropic tides with the differing initial (T, S) fields.

The time—mean depth integrated rate of barotropic to baroclinic energy conversion ($E_{bt\text{-}bc}$) is computed by the equation:

$$E_{bt\text{-}bc} = \left\langle g \int_{-H}^{\eta} \rho' w_{bt} dz \right\rangle,$$

where the angle brackets represent the time average, $w_{bt} = \langle U \rangle \left(\sigma \frac{\partial D}{\partial x} + \frac{\partial \eta}{\partial x} \right) + \langle V \rangle \left(\sigma \frac{\partial D}{\partial y} + \frac{\partial \eta}{\partial y} \right) + \left(\sigma \frac{\partial \eta}{\partial t} + \frac{\partial \eta}{\partial t} \right)$ is the vertical velocity in the Cartesian coordinate associated with the barotropic flow, and ρ' is baroclinic density determined by $\rho' = \rho - \langle \rho \rangle$, where ρ is the instantaneous density. The $E_{bt\text{-}bc}$ is a useful parameter for identifying generation sites of internal tides. The internal tidal energy flux and its depth integration are computed following the method described in Section 6.

Figure 19 illustrates the time—mean, depth integrated internal energy flux and $E_{bt\text{-}bc}$ for the simulated M_2 internal tides. The $E_{bt\text{-}bc}$ suggests the continental shelf break north of the NMH Canyon, particularly near the head of the canyon, and the upper continental slope between NMH Canyon and Mien-Hua Canyon are hot spots for the generation of M_2 internal tides in the ECS. The $E_{bt\text{-}bc}$ is ∼2 W m^{-2} (Figs. 19 a and b). These results are consistent with the results of critical slope analysis (Figs. 7 and 8). A snapshot of horizontal kinetic energy across the shelf and slope at day 5.25 of the model run M2a is shown in Figure 9b. Internal tidal beams are generated on the shelf break and on the critical slope as suggested by the critical slope analysis.

Clearly, the generation of internal tides in the ECS is strongly affected by the stratification profile. Stratification nearing the ECS can be modified by the migration of Kuroshio fronts and by frequent storms in the region. Therefore, it is expected that internal tidal energy and flux vary greatly in time and space, which is supported by our analysis of internal tidal energy and energy fluxes from mooring and EM-APEX float measurements.

The M_2 internal tidal energy flux is ∼5 kW m^{-1} southeastward or southward in the NMH Canyon region and is 5–8 kW m^{-1} emanating northeastward from the I-Lan Ridge. The southeastward energy beam emanating from the NMH Canyon is stronger in the M2a run than in the M2 run, whereas the northeastward energy beam from the I-Lan Ridge is stronger in the M2 run than in the M2a run.

Because the model is forced by the M_2 barotropic tidal forcing, without the S_2, there is no fortnightly cycle of internal tidal energy flux. On the contrary, the observed internal
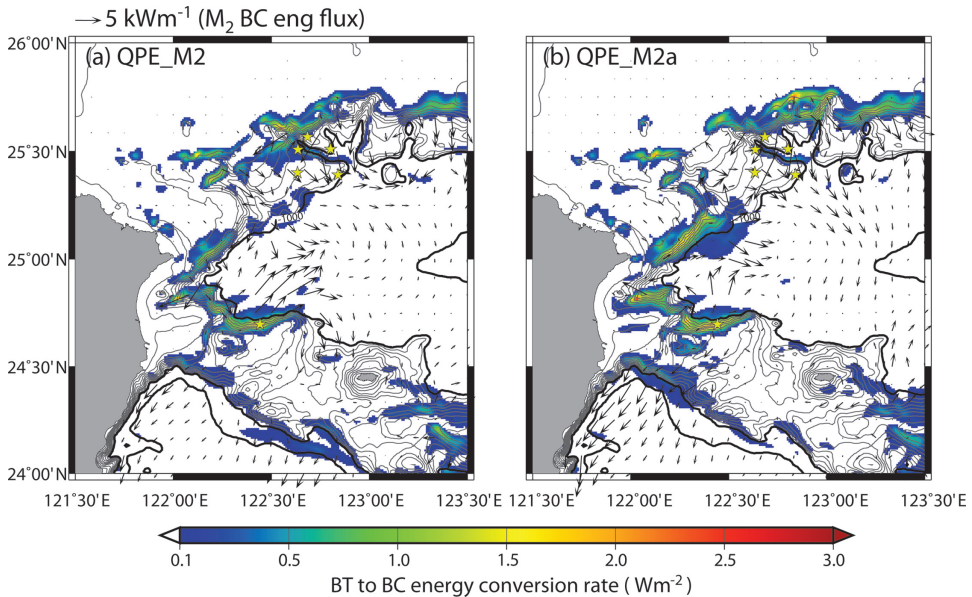
Figure 19. Time averaged and depth integrated rate of barotropic to baroclinic energy conversion (color shading) and energy flux (arrows) for modeled M_2 internal tides. (a) The results of model run1 (M2a) and (b) the results of model run2 (M2). Yellow stars mark the mooring locations. The scale of the energy flux of 5 kW m^{-1} is shown on top of (a).

tidal energy flux shows a strong spring–neap cycle (Fig. 16). Observations suggest that the magnitude of the internal tidal energy flux on the ECS continental slope varies between 3.0 and 10.7 kW m^{-1} averaged over the entire observational period, and between 3.0 and 6.9 kW m^{-1} averaged over the EM-APEX float observational period, is predominantly seaward, and is the strongest at QP4. The modeled magnitude of the internal tidal energy flux varies between 1.0 and 7.2 kW m^{-1}, is predominantly seaward, and is the strongest at QP4. These features agree qualitatively with observations. However, model results of the magnitude and direction of internal tidal energy flux at individual moorings differ significantly from those of observations.

8. Summary

Extensive observations from an array of moorings and EM-APEX floats are analyzed to study the internal waves and internal tides on the continental slope of the ECS. Previous numerical model studies suggest moderate internal tide generation in this region (Niwa and Hibiya, 2001). However, *in-situ* observations are sparse. Our observations provide the detailed properties of internal waves and internal tides on the continental slope of the ECS. Primary findings are summarized as follows:

- High-wavenumber shear layers: Spatially coherent shear layers associated with high-wavenumber semidiurnal internal tides are present over most of the continental slope. They have a dominant vertical scale of $O(100 \text{ m})$ and a horizontal wavelength ~ 7 km, and propagate both upward and downward at $\sim 0.002 \text{ m s}^{-1}$ vertical group speed and at 0.14 m s^{-1} horizontal group speed. Because of their slow propagation speed and strong vertical shear $O(0.01 \text{ s}^{-1})$, they could trigger shear instability, dissipate and provide turbulence mixing on the ECS continental slope.
- Internal tidal energy flux: Both the critical slope analysis and numerical model results suggest that semidiurnal tides are generated on the shelf break, canyon rims and critical slope. Strong spatial and temporal variations of internal tidal energy and internal tidal energy flux are observed, presumably because of the superposition of internal tides from different generation sites. The observed depth integrated semidiurnal internal tidal energy flux varies between 3.0 and 10.7 kW m^{-1}, and propagates predominantly seaward.
- Internal wave energy: Observed total energy in the internal wave continuum is 6.2–13.3 times the GM value. The high energy level is likely attributed to the energy cascade from strong internal tides and inertial waves in the region.

A POM model run to simulate the semidiurnal tidal energy flux forced by the M$_2$ tide yields internal tidal energy averaged over two days at the mooring sites varying between 1.0 and 7.2 kW m^{-1}, propagating predominantly seaward. Model results of the magnitude and direction of internal tidal energy flux at individual moorings differ significantly from observations. The discrepancy between the modeled and observational results may be due to the lack of the S$_2$ tidal forcing, the use of different stratification profiles, the absence of mesoscale processes in the model, insufficient model and bathymetry resolutions or an inaccurate sub-grid parameterization scheme.

Rainville and Pinkel (2004) suggest that the strong positive vorticity of the Kuroshio may block and trap their observed high-wavenumber internal waves between the Kuroshio and continental shelf. A similar blocking effect may be present at the QPE site. Further studies of the spatially coherent shear layers are needed to understand their dynamics and roles in the turbulence mixing.

APPENDIX A

GM frequency spectra

The Garrett and Munk (1972, 1975) internal wave model spectrum has generally been accepted as a reference to compare with observed internal wave spectra in the ocean. The version used in this paper is adopted from genera Cairns and Williams (1976), and referred to as the GM spectrum. The GM frequency spectrum of the total energy $\Phi_E^{GM}(\omega)$, the potential energy spectrum $\Phi_{PE}^{GM} = 1/2N^2\Phi_\eta(\omega)$, the horizontal kinetic energy spectrum $\Phi_{HKE}^{GM}(\omega)$, and the vertical kinetic energy spectrum $\Phi_{VKE}^{GM}(\omega)$ are expressed as

$$\Phi_E^{GM}(\omega) = \Phi_{PE}^{GM}(\omega) + \Phi_{HKE}^{GM}(\omega) + \Phi_{VKE}^{GM}(\omega) = \frac{2}{\pi}b^2 N N_0 E_0 \frac{f}{\omega}\frac{1}{(\omega^2 - f^2)^{1/2}}, \quad (A1)$$

$$\Phi_{PE}^{GM}(\omega) = \frac{1}{\pi}b^2 N N_0 E_0 \frac{f}{\omega}\frac{(\omega^2 - f^2)^{1/2}}{\omega^2}, \quad (A2)$$

$$\Phi_{HKE}^{GM}(\omega) = \frac{1}{\pi}b^2 N N_0 E_0 \frac{f}{\omega}\frac{1}{(\omega^2 - f^2)^{1/2}}\frac{N^2 - \omega^2}{N^2}\frac{(\omega^2 + f^2)}{\omega^2}, \quad (A3)$$

$$\Phi_{VKE}^{GM}(\omega) = \frac{1}{\pi}b^2 N^{-1} N_0 E_0 \frac{f}{\omega}(\omega^2 - f^2)^{1/2}, \quad (A4)$$

where the thermocline exponential scale is chosen as $b = 1.3 \times 10^3$ m, the reference buoyancy frequency $N_0 = 5.2 \times 10^{-3}\mathrm{s}^{-1} = 3$ cph, and the non-dimensional GM energy parameter $E_0 = 6.3 \times 10^{-5}$. The GM rotary clockwise spectrum $\Phi_{CW}^{GM}(\omega)$ and counter-clockwise spectra $\Phi_{CCW}^{GM}(\omega)$ can be expressed as

$$\Phi_{CW}^{GM}(\omega) = \frac{1}{\pi}b^2 N N_0 E_0 \frac{f}{\omega}\frac{1}{(\omega^2 - f^2)^{1/2}}\frac{N^2 - \omega^2}{N^2}\frac{(\omega + f)^2}{\omega^2}, \quad (A5)$$

$$\Phi_{CCW}^{GM}(\omega) = \frac{1}{\pi}b^2 N N_0 E_0 \frac{f}{\omega}\frac{1}{(\omega^2 - f^2)^{1/2}}\frac{N^2 - \omega^2}{N^2}\frac{(\omega - f)^2}{\omega^2}. \quad (A6)$$

APPENDIX B

Consistency relations for linear internal waves

Fofonoff (1969) and Müller et al. (1978) derived consistency relations for random linear internal waves. These consistency relations are derived from the dispersion and polarization relations of linear internal waves, assuming spatial homogeneity. Two consistency relations used in the present analysis are (1) the ratio of the counterclockwise velocity (CCW) spectrum to the clockwise velocity (CW) spectrum, and (2) the ratio of the potential energy (PE) spectrum to the horizontal kinetic energy (HKE) spectrum; they are expressed as

$$\gamma_{CCW/CW} = \frac{\Phi_{CCW}(\omega)}{\Phi_{CCW}(\omega)} = \frac{(\omega - f)^2}{(\omega + f)^2}, \quad (B1)$$

$$\gamma_{PE/HKE} = \frac{\Phi_{PE}(\omega)}{\Phi_{HKE}(\omega)} = \frac{N^2}{N^2 - \omega^2} \frac{\omega^2 - f^2}{\omega^2 + f^2}. \tag{B2}$$

For vertical standing linear internal waves, the consistency relation (B1) is still valid, but the consistency relation (B2) is not (Müller et al., 1978). Using the polarization relation and dispersion relation of linear internal waves, we find that the ratio of PE to HKE frequency spectra for the vertical standing mode $\gamma^*_{PE/HKE}$ varies with the vertical wavenumber (m) and depth (z) as

$$\gamma^*_{PE/HKE} = \frac{\Phi_{PE}(\omega)}{\Phi_{HKE}(\omega)} = \frac{N^2}{N^2 - \omega^2} \frac{\omega^2 - f^2}{\omega^2 + f^2} \frac{\sin^2(mz)}{\cos^2(mz)}. \tag{B3}$$

For the first mode internal wave in the ocean of a constant N, $m = \pi/H$, where H is the ocean depth. The vertical displacement, thereby the potential energy, vanishes at the sea surface and bottom. The horizontal velocity vanishes at the mid-depth. Therefore, the ratio PE/HKE is zero at the sea surface and bottom, and becomes infinity at the mid-depth.

APPENDIX C

Decomposition of upward and downward propagating waves

Mooring observations of temperature, salinity, density and velocity as a function of (z, t), where z is the vertical coordinate and t is time, can be represented in Fourier space (ω, m) as a superposition of vertically propagating waves, where ω is frequency and m is vertical wavenumber, i.e.,

$$\psi(t, z) = \int_{-\infty}^{\infty} d\omega \int_{-\infty}^{\infty} dm \ \hat{\psi}(\omega, m)e^{i(\omega t - mz)}. \tag{C1}$$

The reality condition of observations $\psi(t, z)$ implies $\hat{\psi}^*(\omega, m) = \hat{\psi}(-\omega, -m)$. In the Fourier space, waves with positive frequency and negative wavenumber, and waves with negative frequency and positive wavenumber represent waves of downward phase propagation (upward energy propagation), i.e.,

$$\Psi^{down}(t, z) = \int_0^{\infty} d\omega \int_{-\infty}^0 dm \ \hat{\psi}(\omega, m)e^{i(\omega t - mz)} + \int_{-\infty}^0 d\omega \int_0^{\infty} dm \ \hat{\psi}(\omega, m)e^{i(\omega t - mz)}. \tag{C2}$$

Similarly, waves with positive frequency and positive wavenumber, and waves with negative frequency and negative wavenumber represent waves of upward phase propagation (downward energy propagation), i.e.,

$$\psi^{up}(t, z) = \int_0^{\infty} d\omega \int_0^{\infty} dm \ \hat{\psi}(\omega, m)e^{i(\omega t - mz)} + \int_{-\infty}^0 d\omega \int_{-\infty}^0 dm \ \hat{\psi}(\omega, m)e^{i(\omega t - mz)}. \tag{C3}$$

This linear decomposition assures that $\psi(t, z) = \psi^{up}(t, z) + \psi^{down}(t, z)$.

REFERENCES

Alford, E. H. and Z. Zhao. 2007. Global patterns of low-mode internal-wave propagation. Part II: Group velocity, J. Phys. Oceanogr., *37*, 1849–1858.

Bains, P. G. 1982. On internal tide generation models, Deep-Sea Res., *29*, 307–338.

Blumberg, A. F. and L. H. Kantha. 1985. Open boundary condition for circulation models. J. Hydra. Eng., *111*, 2, 237–255.

Blumberg, A. F. and G. F. Mellor. 1987. A description of a three dimensional coastal ocean circulation model, *in* Three-Dimensional Coastal Ocean Models, Coastal and Estuarine Stud., vol. 4, N. Heaps, ed., AGU, Washington D.C., 1–16.

Cairns, J. L. and G. D. Williams. 1976. Internal wave observations from a midwater float, Part II, J. Geophys. Res., *81*, 1943–1950.

Duda, T. F. ; A. E. Newhall; G. Gawarkiewicz; M. Caruso; H. Graber; Y.-J. Yang and S. Jan. 2013. Significant internal waves and internal tides at a shelf edge and canyon region northeast of Taiwan, J. Mar. Res., *71*(1–2), 47–82.

Egbert, D. G. and S. Y. Erofeeva. 2002. Efficient inverse modeling of barotropic ocean tides, J. Atmos. Oceanogr. Technol., *19*, 183–204.

Eriksen, C. C. 1982. Internal observations of internal wave reflection off sloping bottoms, J. Geophys. Res., *87*, 525–538.

Fofonoff, N. P. 1969. Spectral characteristics of internal waves in the ocean, Deep-Sea Res., *16* (Suppl.), 58–71.

Garrett, C. J. and W. Munk. 1972. Space–time scales of internal waves. Geophys. Fluid Dyn., 2, 255–264.

Garrett, C. J. and W. Munk. 1975. Space–time scales of internal waves: A progress report. J. Geophys. Res., *80*, 291–297.

Garrett, C. J. and E. Kunze. 2007. Internal tide generation in the deep ocean. Ann. Rev. Fluid Mech., 39, 57–87.

Gawarkiewicz, G.; S. Jan; P. F. J. Lermusiaux; J. L. McClean; L. Centurioni; K. Taylor; B. Cornuelle; T. F. Duda; J. Wang; Y.J. Yang; T. Sanford; R.-C. Lien; C. Lee; M.-A. Lee; W. Leslie; P. J. Haley Jr.; P. P. Niiler; G. Gopalakrishnan; P. Velez-Belchi; D.-K. Lee and Y. Y. Kim. 2011. Circulation and intrusions northeast of Taiwan: Chasing and predicting uncertainty in the cold dome. *Oceanography, 24*, 110–121.

Gregg, M. C. 1989. Scaling turbulent dissipation in the thermocline. J. Geophys. Res., *94*, 9686–9698.

Hotchkiss, F. S. and C. Wunsch. 1982. Internal waves in Hudson Canyon with possible geological implications. Deep-Sea Res., *29*, 415–442.

Hu, C.-K.; C.-T. Chiu; S.-H. Chen; J.-Y. Kuo; S. Jan and Y.-H. Tseng. 2010. Numerical simulation of barotropic tides around Taiwan. Terr. Atmos. Ocean. Sci., *21*, 1, 71–84, doi: 10.3319/TAO.2009.05.25.02(IWNOP).

Jan, S; R.-C. Lien and C.-H. Ting. 2008. Numerical study of baroclinic tides in Luzon Strait. J. Oceanogr., *64*, 5, 789–802.

Jan, S. and C. T. A. Chen. 2009. Potential biogeochemical effects from vigorous internal tides generated in the Luzon Strait: A case study at the southernmost coast of Taiwan. J. Geophys. Res., *114*, C04021, doi:10.1029/2008JC004887.

Jan, S.; J. Wang; Y. J. Yang; C.-C. Hung; C.-S. Chern; G. Gawarkiewicz; R.-C. Lien; L. Centurioni; J.-Y. Kuo and B. Wang. 2013. Observation of Typhoon Morakot-induced freshwater pulse off northern Taiwan in August 2009. J. Mar. Res., *71*(1–2), 19–46.

Klymak, J. M.; J. N. Moum; J. D. Nash; E. Kunze; J. B. Girton; G. S. Carter; C. M. Lee; T. B. Sanford and M. C. Gregg. 2006. An estimate of tidal energy lost to turbulence at the Hawaiian Ridge. J. Phys. Oceanogr., *36*, 1148–1164.

Kunze, E.; L. K. Rosenfeld; G. S. Carter and M. C. Gregg. 2002. Internal waves in Monterey Submarine Canyon. J. Phys. Oceanogr., *32*, 1890–1913.

Lee, C. M.; E. Kunze; T. B. Sanford; J. D. Nash; M. A. Merrifield and P. E. Holloway. 2006. Internal tides and turbulence along the 3000 m isobath of the Hawaiian Ridge. J. Phys. Oceanogr., *36*, 1165–1183.

Lien, R.-C. and M. C. Gregg. 2001. Observations of turbulence in a tidal beam and across a coastal ridge. J. Geophys. Res., *106*, 4575–4591.

Lueck, R. G. and T. D. Mudge. 1997. Topographically induced mixing around a shallow seamount. Science, *276*, 1831–1833.

Martinsen, E. H. and H. Engedahl. 1987. Implementation and testing of a lateral boundary scheme as an open boundary condition in a barotropic ocean model. Coast. Eng., *11*, 603–627.

Mellor, G. L. and T. Yamada. 1982. Development of a turbulence closure model for geophysical fluid problems. Rev. Geophys. Space Phys., *20*, 851–875.

Müller, P.; D. J. Olbers and J. Willebrand. 1978. The Iwex Spectrum. J. Grophys. Res., *83*, 479–500.

Müller, P. 1988. Vortical motions, *in* Small-Scale Turbulence and Mixing in the Ocean, J. C. J. Nihoul and B. Jamart, eds., Elsevier Science Publishers, 285–302.

Nash, J. D.; M. H. Alford and E. Kunze. 2005. Estimating internal waves energy fluxes in the ocean. J. Atmos. Ocean. Technol., *22*, 1551–1570.

Niwa, Y. and T. Hibiya. 2001. Numerical study of the spatial distribution of the M2 internal tides in the Pacific Ocean. J. Geophys. Res., *106*, 22441–22449.

Qiu B. and N. Imasato. 1990. A numerical study on the formation of the Kuroshio Counter Current and the Kuroshio Branch Current in the East China Sea. Cont. Shelf. Res., 165–184.

Rainville, L. and R. Pinkel. 2004. Observations of energetic high-wavenumber internal waves in the Kuroshio. J. Phys. Oceanogr., *34*, 1495–1505.

Sanford, T. B.; J. H. Dunlap; J. A. Carlson; D. C. Webb and J. B. Girton. 2005. Autonomous velocity and density profiler: EM-APEX. *Proceedings of the IEEE/OES Eighth Working Conference on Current Measurement Technology*, IEEE Cat No. 05CH37650, ISBN: 0-7803-8989-1, 152–156.

Smagorinsky, J. 1963. General circulation experiments with the primitive equations: I. The basic experiments. Mon. Wea. Rev., *91*, 99–164.

van Haren, H.; L. Mass and H. van Aken. 2002. On the nature of internal wave spectra near a continental slope. Geophys. Res. Lett., *29*, 12, 1615, 10.1029/2001GL014341.